Article
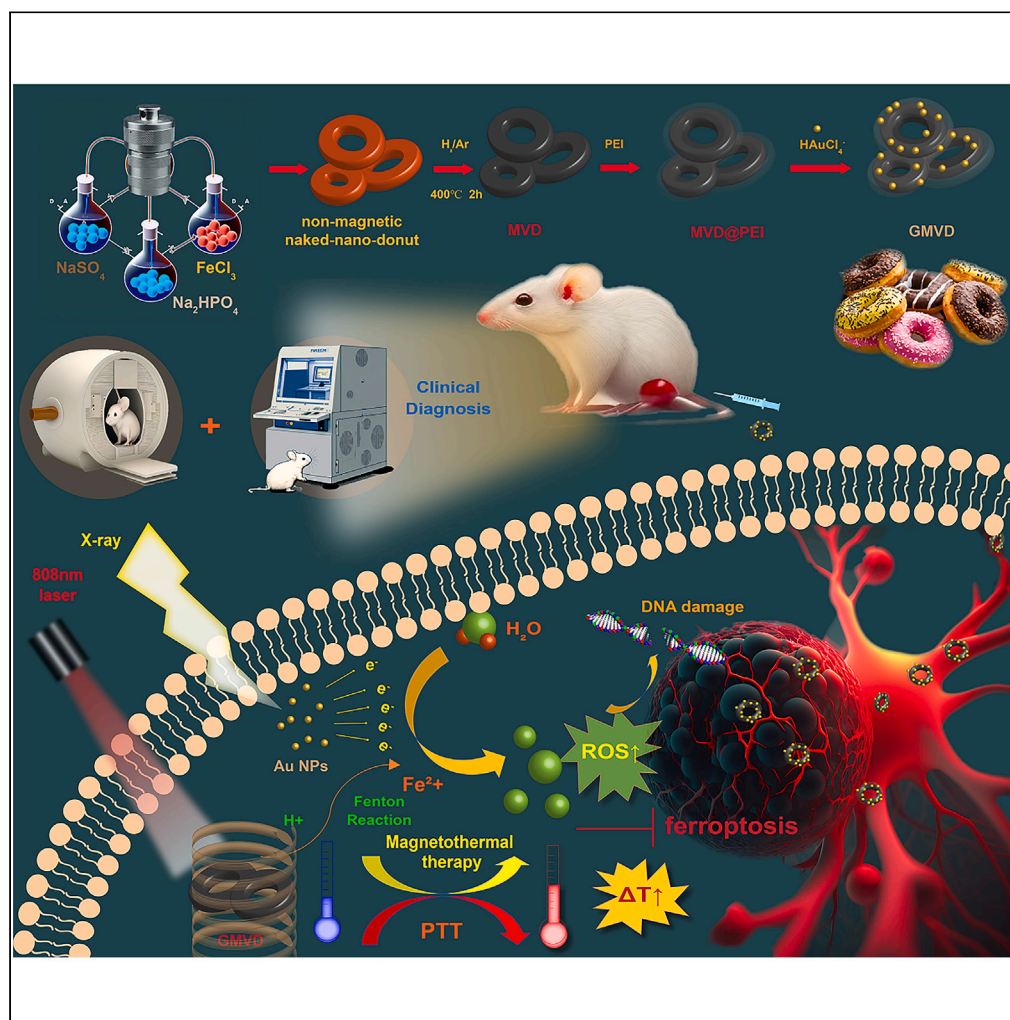
Magnetic-vortex nanodonuts enhance ferroptosis effect of tumor ablation through an imaging-guided hyperthermia/radiosensitization strategy

S.S. Guo, M.M. Chen, Y.H. Yang, ..., D.D. Fan, J.F. Bao, Z.Y. Ji

dandanfan0725@163.com (D.D.F.)
baoguojianfeng@gmail.com (J.F.B.)
jizhenyu@zzu.edu.cn (Z.Y.J.)

Highlights

Successfully synthesized a theranostics gold-modified magnetic vortex donut (GMVD)

GMVD exhibits high photothermal conversion efficiency for hyperthermia of tumors

Photothermal-triggered GMVD produced ROS, which enhanced the tumor ferroptosis effect

GMVD increases tumor radiosensitivity, thereby further improving tumor ablation

Article

Magnetic-vortex nanodonuts enhance ferroptosis effect of tumor ablation through an imaging-guided hyperthermia/radiosensitization strategy

S.S. Guo,[1] M.M. Chen,[1] Y.H. Yang,[1] Y.Y. Zhang,[1] X. Pang,[3] Y.P. Shi,[2] Y.C. Zhuang,[4] D.D. Fan,[1,*] J.F. Bao,[2,*] and Z.Y. Ji[1,5,*]

SUMMARY

Pursuing more efficient multifunctional treatment is the main challenge of preclinical nanoparticle-mediated theranostics research. Here, nanoscale magnetite vortex donut shape was synthesized as a platform, and then ultrasmall gold nanoparticles were successfully embedded into the nanoring surface, thereby obtaining gold-modified magnetic vortex donut (GMVD). GMVD has a high photothermal conversion efficiency (η = 42.2%), which makes it have excellent photothermal ablation effect on tumors both *in vivo* and *in vitro*. Simultaneously, GMVD forms reactive oxygen species (ROS) under the 808 nm laser triggering, inducing ferroptosis. The addition of gold element also makes GMVD have the effect of radiotherapy (RT) sensitization. In conclusion, the synergistic treatment of RT and PTT greatly enhanced tumor ablation, indicating that GMVD has good biocompatibility and antitumor efficacy. This work demonstrates that the proposed GMVD can be a high-performance tumor diagnosis and theranostic treatment agent and may have great potential for clinical application in the future.

INTRODUCTION

Globally, cancer is considered the second leading cause of death as an aggressive and malignant disease.[1] Current cancer therapies, such as surgical resection, chemotherapy, and radiation therapy (RT), have serious limitations.[2] Among them, RT uses high-energy ionizing radiation, such as gamma rays or X-rays, to kill cancer cells by ionizing cellular components and/or water to produce cytotoxic free radicals (like the reactive oxygen species, ROS) to attack DNA-like bioactive macromolecules in cancer cells.[3] However, the X-ray absorption rate of solid tumors is usually unsatisfactorily low; therefore, patients must receive excessive radiation doses, which inevitably cause severe damage to normal tissues.[4] In addition, repeated radiotherapy stimulates mutations in cancer cells, leading to the development of treatment resistance.[5] To overcome the deficiencies of radiotherapy, a series of radiosensitizers, usually heavy atom nanoparticles, such as gold (Au),[6] bismuth (Bi),[7] rare earth,[8] and platinum (Pt)[9] have been significantly developed. They have higher X-ray absorption capacity and the photoelectric effect, which allows precisely localized enhanced therapeutic efficacy at relatively lower and safer radiation doses. Therefore, radiosensitizers have become promising nanoformulations for tumor radiotherapy.[10,11]

Hyperthermia has recently been introduced as an adjuvant therapy for cancer and holds great promise in combating this disease.[12] Hyperthermia is defined as a treatment method that exposes target tissue to high temperatures that directly damage the tissue (thermal ablation at temperatures above 47°C) or make cancer cells more susceptible to other treatment modalities (mild heat therapy in the temperature range 41°C–45°C).[13] Among various heating strategies, alternating magnetic field (AMF) and near-infrared (NIR)-induced hyperthermia is the most studied and generally considered the most suitable methods.[14,15] Magnetothermal therapy (MTT) uses magnetothermal agents to convert magnetic energy into heat in AMF for tumor ablation. Magnetic nanoparticles (MNPs) have been considered ideal magnetothermal agents, and a variety of different Fe-based nanoparticles have been confirmed to have an excellent magnetothermal effect and can well cause tumor regression, such as iron oxide nanospheres,[16] magnetic nanocrystals of Mn-Zn ferrite,[17] Fe-Mn nanoflowers[18] and so on. However, the low hyperthermia conversion efficiency of clinically used magnetothermal agents makes the treatment dose too large, which brings potential side effects to patients, thus greatly limiting the broad application of magnetothermal therapy.[19] Therefore, developing MNPs with higher specific absorption rates (SAR) will greatly solve the existing problems. On the other hand, photothermal therapy (PTT) utilizes the photothermal effect of photothermal agents (PTA) to convert absorbed light energy into heat, causing thermal burns on tumors.[20] PTT has been paid

[1]Henan Institute of Medical and Pharmaceutical Sciences, Zhengzhou University, Zhengzhou 450000, China
[2]Functional Magnetic Resonance and Molecular Imaging Key Laboratory of Henan Province, Department of Magnetic Resonance Imaging, The First Affiliated Hospital of Zhengzhou University, Zhengzhou University, Zhengzhou 450000, China
[3]School of Pharmacy, Henan University of Chinese Medicine, Zhengzhou 450000, China
[4]Department of Imaging Sciences, University of Rochester Medical Center, Rochester, NY, USA
[5]Lead contact
*Correspondence: dandanfan0725@163.com (D.D.F.), baoguojianfeng@gmail.com (J.F.B.), jizhenyu@zzu.edu.cn (Z.Y.J.)
https://doi.org/10.1016/j.isci.2024.110533

attention to because of its simple operation, short treatment time, and quick recovery.[21,22] Various NIR-dependent photothermal nanomaterials have been used as PTA, such as Au-based nanostructures,[23] carbon-based nanocomposites[24] and Pd-based nanostructures,[25] etc. Au-based NPs have strong absorbance in the NIR, thus showing great potential in photothermal therapy.[26]

By combining different therapeutic agents, contrast agents or targeting agents on the surface of nanoparticles, medical diagnosis and drug delivery are integrated into a single nanoplatform,[27] which constitutes an integrated nanoplatform for diagnosis and treatment, which has aroused widespread interest in the field of nanomedicine.[28–30] magnetic iron oxide NPs have been used in magnetic resonance (MR) imaging due to their T_2 shortening effect[31] and Au NPs with specific shapes can strongly absorb NIR light for photoacoustic imaging (PAI).[32,33] Considering all the properties mentioned above and capabilities of magnetic iron oxide NPs and AuNPs, they can be combined into a nanocomposite.[34]

Based on these analyses, we present a biocompatible gold-decorated magnetic-vortex nano-donut (GMVD), which becomes an MRI/PAI-guided magnetothermal/photothermal/radiotherapy sensitization theranostics nanoparticles. After identification, GMVD has a shape characteristic similar to a donut. The magnetic vortex iron oxide with a special structure is like a naked donut bread body, and the extremely small gold particles cover its entire surface like sugar grains. The unique magnetic donut structure endows GMVD with an excellent specific absorption rate (SAR_{PTT} = 1747.48 W/g, SAR_{MTT} = 1222.65 W/g), and the addition of gold nanoparticles makes the photothermal conversion efficiency reach an astonishing 42.2%. Validated in cancer cells, GMVD exhibited excellent contrast agents for T_2-weighted magnetic resonance imaging, PAI enhancement, specific laser-induced PTT toxicity, and sensitization of cells to X-ray radiotherapy. A more encouraging finding is that photothermal triggers GMVD to enhance ROS production, leading to ferroptotic iron metabolism. Furthermore, the combination of PTT and RT resulted in synergistic effects, significantly inhibiting the growth of 4T1 tumors. And we preliminarily explored the caspase3/9 apoptosis pathway as the critical mechanism of tumor regression. Our results indicate that GMVD have the potential to be promising candidates for cancer diagnostic imaging and therapy.

RESULTS

Synthesis and preparation of GMVD

As shown in Scheme 1, GMVD was synthesized. According to previous studies,[35] first, a uniform morphology oil bath was used to obtain magnetic vortex naked-nano-donut (Figure S1). Its unique ring structure gives it a bigger specific surface area to combine other substances. In the presence of polyethyleneimine, tiny colloidal gold particles were dispersedly covering the naked-nano-donut surface, which was clearly visible under TEM (Figure 1A). The diameter of GMVD in TEM was measured using ImageJ software. The GMVD's average inner diameter was about 58.7 nm, and the average outer diameter was about 141.0 nm. The diameter of GMVD was found to be similar by DLS measurement (Figure S2), which was about 114 nm. In addition, the distribution of GMVD in FBS was relatively stable, and the particle size increased to 280.7 nm after 5 days Figure 1B is a scanning TEM (STEM) image of a typical Magnetic vortex nano-donut, on which elemental mapping analysis was induced. It shows STEM-energy dispersive X-ray (STEM-EDX) elemental mapping of Fe, O and Au, respectively. Fe and O elements form a ring, with tiny gold elements randomly covering the outer surface of the ring, confirming a structure like a donut dusted with powdered sugar. Moreover, the high-resolution TEM (HRTEM) image (Figure S3) shows the lattice fringes of Fe_3O_4 (~2.54 Å) and Au (~2.43 Å), respectively, corresponding to the (3 3 1) plane of Fe_3O_4 and the (2 0 0) plane of Au. X-ray powder diffraction (XRD, Figure 1C) further verified that GMVD were crystalline, and the diffraction peaks were unambiguously indexed into magnetic iron oxide (JCPDS 88–0866) and Au (JCPDS 99-0056), respectively. And Energy Dispersive Spectroscopy (EDS) shows that the mass fraction of Au in GMVD is about 23.139% (Figure S4). X-ray photoelectron spectroscopy (XPS) was used to characterize the addition of Au (Figure 1D). The Survey map shows that there are C, O, Fe, and Au elements in GMVD. In addition, according to the XPS spectrum of Fe 2p, the XPS peaks at 710.11 eV and 721.73 eV correspond to the characteristic peaks of Fe 2p 3/2 and Fe 2p 1/2, indicating the presence of Fe^{3+} in GMVD. The two peaks 87.68 and 83.98 eV of the Au narrow spectrum scan are attributed to Au 4f 5/2 and Au 4f 7/2 in Au0 respectively; the O spectrum peak 530.08 eV corresponds to O1 s in Fe_3O_4. It was proved that the composite material is composed of Au and Fe_3O_4. As shown in Figure 1E, the saturation magnetization (Ms) of the obtained GMVD was 51.4 emu/g. Due to the non-magnetic Au and PEI polymer matrix, it was lower than the value of MVD at 104.3 emu/g.[36] However, this value of GMVD still has a higher saturation magnetization value to be suitable for clinical application. At the same time, due to the larger particle size, GMVD exhibits higher magnetic susceptibility and saturation magnetization than the superparamagnetic particles, indicating that favorable transverse relaxation effects could be expected, and the proposed GMVD may also have great potential in MRI-guided tumor therapy. By comparing the UV-visible absorption spectra (Figure 1F), compared with MVD, GMVD of the same concentration has higher UV absorption at 808 nm, which means it has higher photothermal potential. Interestingly, MVD has a characteristic absorption peak at around 410 nm, which disappears after PEI modification and loading of Au particles. This may be due to the strong surface plasmon coupling effect between adjacent Au on MVD's surface, which causes the spectrum to red shift.[37,38] In addition, with the addition of PEI, the zeta potential of GMVD becomes negative (Figure S2). Due to the positive charge on the surface of tumor cell membranes, nanoparticles with negative zeta potential are more easily taken up by tumor cells and have higher biocompatibility.[39]

In vitro magnetothermal/photothermal effect

We then studied the thermogenic capacity of GMVD under 808 laser and AMF. A dispersion of GMVD at a concentration of 75 μg/mL was irradiated with an 808-nm laser with a power density from 0.7 to 1.9 W/cm², and it was found that at the minimum power of 0.7W/cm², GMVD can still heat up to 56.7°C (Figures 2A and 2C). Furthermore, a series of GMVD dispersions with concentrations ranging from 0.0 to 150 μg/mL in water were irradiated with an 808-nm laser at a power density of 0.9 W/cm² for 10 min. Through the calculation of the temperature rise at a
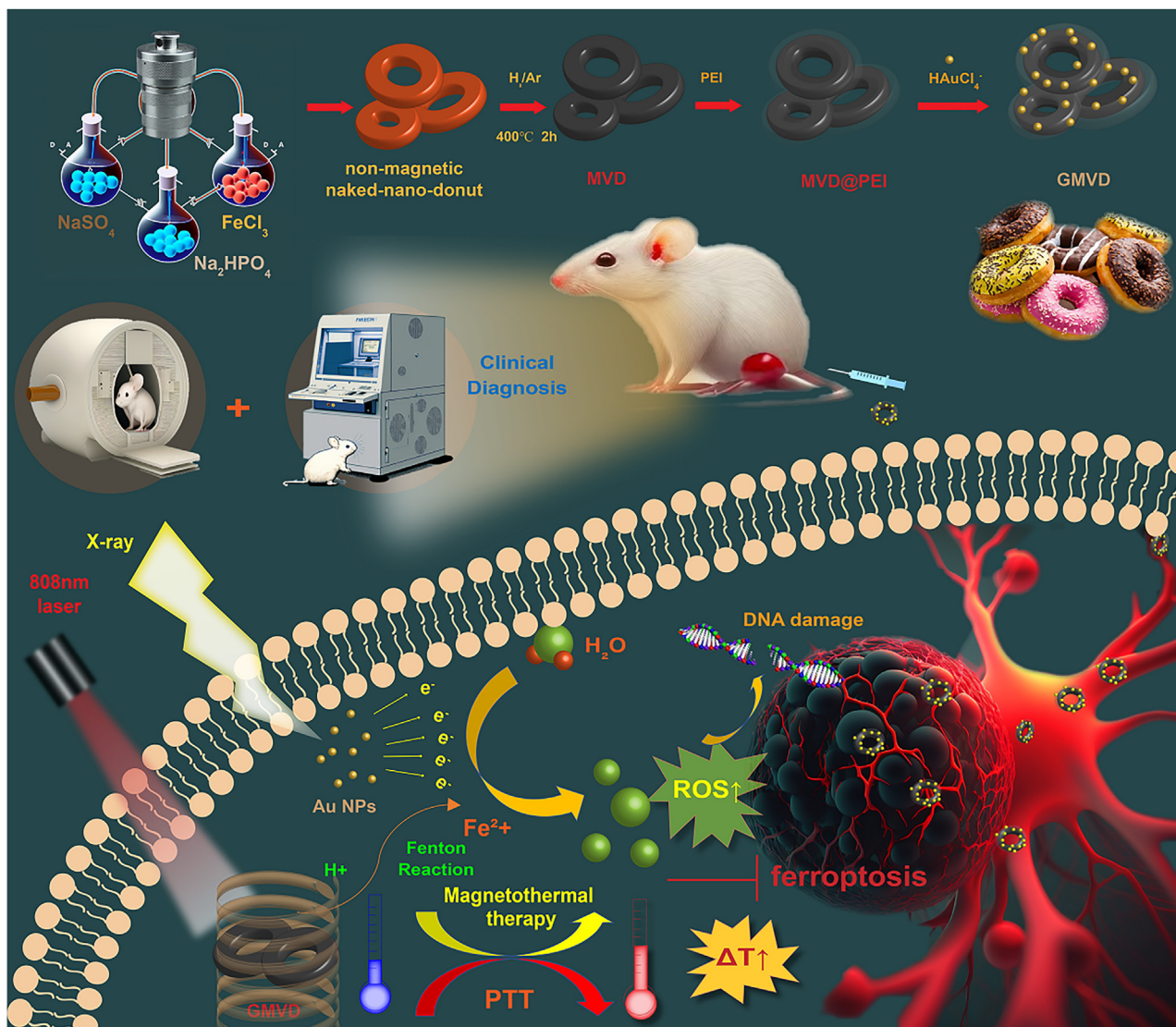
Scheme 1. Schematic illustration for the formation of GMVD and T$_2$-weighted MRI/PAI-guided dual-thermal enhanced radiation synergistic therapy
GMVD was synthesized by a hydrothermal method. After specific NIR laser and X-ray irradiation on the tumor site, GMVD can cause tumor ablation. At the same time, PTT triggers an enhancement of the Fenton response, releases ROS, and triggers ferroptosis.

power of 1.9 W/cm^2, it can be seen that the photothermal SAR value of GMVD is as high as 1747.48 W/g. The color-coded images (Figure S5A) and the corresponding curves for temperature changes (Figure S5B) show that all the GMVD dispersions experienced significant temperature increases within 120 s of turning on the laser. Notably, even the dispersion with the lowest concentration of GMVD (38 μg/mL) reached above 50.4°C after 300 s of laser irradiation, sufficient to induce irreversible cell apoptosis due to hyperthermia.[10] After turning off the laser, the suspension rapidly cooled down below physiological temperature (37°C) within 180 s (Figure 2E). When the laser was turned on again, the nanoparticles raised to a similar temperature at a similar speed, which can last more than 5 cycles, proving that the material has good repeated photothermal properties (Figure 2G). The photothermal conversion efficiency (η) of GMVD was then calculated to be 42.2%, demonstrating its excellent photothermal conversion ability (Figure 2F).

GMVD also has excellent heating ability under AMF (Figures S6 and S7). Compared with spherical magnetic iron oxide nanoparticles, under the same power of AMF, the heating capacity of GMVD is about 10°C higher than that of nanosphere-Fe$_3$O$_4$ (Figures 2B and 2D). After calculation, GMVD also has a high magnetothermal SAR value of 1222.65 W/g. Due to the unique ring structure of GMVD, the magnetization reversal of the vortex-onion state occurs in the presence of a magnetic field, resulting in a large hysteresis, which makes GMVD have an order of magnitude higher magnetothermal efficiency than traditional superparamagnetic iron oxide.[40]

In summary, whether it is photothermal or magnetic thermal, GMVD performs outstanding and has great potential.
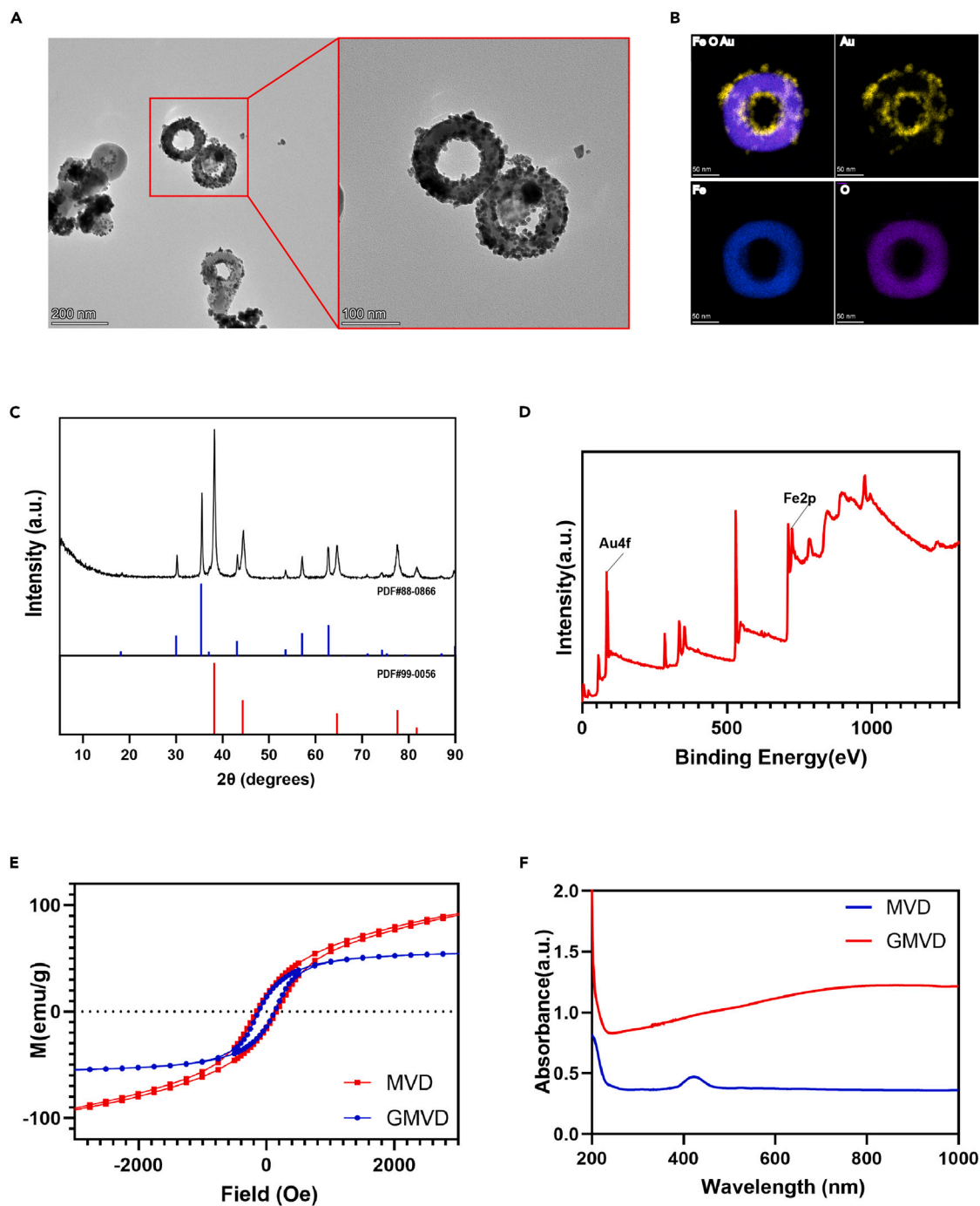
**Figure 1. Successful synthesis and characterization of GMVD**

(A) TEM image of GMVD, scale bar = 200/100 nm.

(B) EDS mapping images of all overlapping elements.

(C) X-ray powder diffraction (XRD) spectrum of GMVD and corresponding fingerprints of crystalline indexes for magnetic iron oxide (JCPDS 88–0866) and Au (JCPDS 99-0056).

(D) X-ray Photoelectron Spectroscopy (XPS) image of GMVD.

(E) Magnetic hysteresis loops of MVD (red), GMVD (blue); (F) UV absorption curves of MVD (blue), GMVD (red).
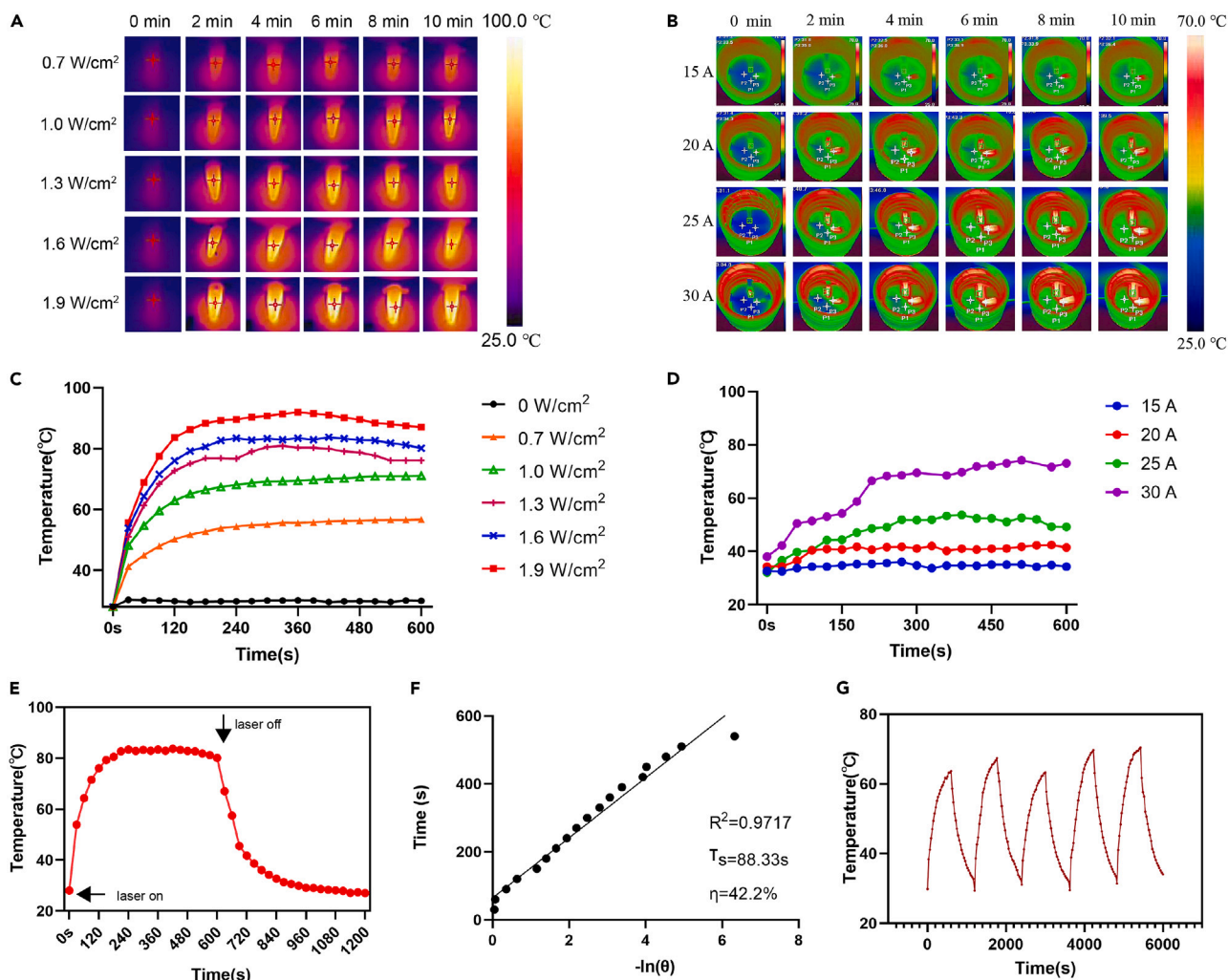
Figure 2. GMVD has good photothermal and magnetothermal properties

(A) Representative thermal images of 75 μg/mL GMVD dispersion in water during laser irradiation at 0.7–1.9 W/cm².

(B) Thermal images of water (left), non-magnetic naked-nano-donut (bottom, [Fe] = 5 mg/mL), nanospheres-Fe_3O_4 (right, [Fe] = 5 mg/mL), GMVD (top, [Fe] = 5 mg/mL) at AMF (15–30 A).

(C) The corresponding temperature change curve of photothermal therapy.

(D) The corresponding temperature change curve of magnetic hyperthermia therapy.

(E) Temperature evolution of GMVD solution under irradiation.

(F) The photothermal conversion efficiency of GMVD.

(G) The photothermal temperature change curve of laser on-off five cycles.

In vitro cytotoxicity and cellular uptake

It is worth noting that the microscopic morphology of MVD induces the magnetic vortex effect, resulting in our synthesized material exhibiting remarkable magnetocaloric properties. These properties have been previously demonstrated in relevant studies[41] and confirmed through *in vitro* experiments conducted in this study. Building upon these findings, our research aims to investigate whether the magnetocaloric properties of gold nanoparticles remain largely unaffected after modification. Additionally, this multifunctional nano-platform possesses a broader range of antitumor properties that complement its magnetocaloric functionality. Considering this fundamental platform's widely reported excellent magnetocaloric performance, we have excluded magnetocaloric heat treatment from the cell and animal studies from avoiding any potential confusion and focusing solely on verifying the modified performance and emphasizing its complementary relationship with magnetocaloric effects.

In order to prove that GMVD has a good photothermal effect in addition to the magnetocaloric effect, we selected four different cancer cell lines for verification. Similarly, GMVD showed cell killing effects in the 4T1 (mouse breast cancer cell), HeLa (human cervical cancer cell), KYSE-150 (human esophageal squamous cell carcinoma cell), and A-375 (human malignant melanoma cell). These were after the irradiation of

808 nm laser and increases with the increase of GMVD's concentration. Without the use of laser, GMVD does not affect the normal growth of cells and shows good biocompatibility. (Figure 3A). The results show that GMVD not only has a killing effect on specific tumor cells but also is effective on a broad spectrum of tumor cells, which provides the possibility for more applications in the future. In addition, the above-mentioned good photothermal effect is largely due to the addition of gold. Through ICP-OES, the mass fraction of gold in GMVD is approximately 27.7145%, which is very close to the result of the EDS test. When tested under the same content of MVD, it can be found that the photothermal activity of GMVD is better than that of MVD at each concentration (Figure S8), indicating that although gold is added in ultra-small particles, the sufficient content gives it sufficient specific surface area to enhance the photothermal activity.

For subsequent *in vitro* experiments, we selected HeLa cells as representatives for experiments. What's more, as shown in Figure 3B, the thin-section cell TEM images further prove that the GMVD incubated in cells were taken up through the endocytic pathway. Cell viability was observed by Calcein-AM/PI live/dead cell staining (Figures 3C and S9): more than 95% of cells were PI-positive after the treatment with PTT +300 μg/mL GMVD. These results show that the GMVD can be well non-specifically absorbed by a variety of tumor cells and exert excellent photothermal effects to cause damage to tumor cells.

Photothermal-triggered ferroptosis-inducing ability of GMVD

Since iron itself is a key component in the production of ROS by the Fenton reaction, the process of ferroptosis is inseparable from the participation of iron.[42] Therefore, we speculate that GMVD can serve as an iron ion supplier, enhance the production of ROS, and participate in iron metabolism in ferroptosis. However, GMVD itself has good biocompatibility and will not directly kill cells. The induced ferroptosis needs to be triggered by exogenous factors such as light and heat.[43] We observed the phenomenon of ROS production in GMVD after PTT by laser confocal microscopy, and found that the generation of intracellular Fe^{2+} ions also increased by FerroOrange staining assay (Figure S10). We preliminarily speculated that GMVD may trigger ferroptosis of tumor cells through hyperthermia.

Ferroptosis is defined as a process of programmed cell death caused by the accumulation of iron-dependent lipid peroxidation (LPO).[44] Ferroptosis is morphologically, biochemically, and genetically distinct from apoptosis, necrosis, and other modalities of regulated cell death. A large number of studies[45–47] have confirmed that ferroptosis plays a key therapeutic role in various malignant tumors such as liver cancer, colorectal cancer, breast cancer, and hematological malignancies. The ferroptosis process is characterized by the accumulation of LPO and lethal ROS from iron metabolism, and can be inhibited by iron chelators. Iron catalyzes the production of ROS through the Fenton reaction, which is an important way to induce ferroptosis. Excess ferrous iron can provide electrons to promote lipid peroxidation through the Fenton reaction and generate ROS, thereby inducing ferroptosis.[48]

In order to verify whether photothermal triggers the ferroptosis pathway induced by GMVD, we performed RNA sequencing on cells treated with GMVD combined with PTT (Figure 4A). Based on the sequencing results, we performed an enrichment analysis through Database:Kyoto Encyclopedia of Genes and Genomes (KEGG), and found that ferroptosis is a significant change pathway, and the *p* value (*p* = 0.0285) is smaller than that of the apoptotic pathway (*p* = 0.0305). It was proved that after photothermal triggering, GMVD induced cell death mainly involving ferroptosis.

Subsequently, the GMVD-induced ferroptosis pathway was verified in cells. The ferroptosis pathway induced by GMVD was subsequently verified in cells. 4T1 cells after PTT obviously produced a large amount of ROS (Figure 4B). Lipid peroxidation produces two natural products, namely malondialdehyde (MDA) and 4-hydroxynonenal (4-HNE); measuring the final products of lipid peroxidation is an effective measurement method that reflects oxidative damage. Use relevant kits to detect intracellular MDA content, and its content is positively correlated with ferroptosis. In particular, ferroptosis can be inhibited by Ferrostatin-1 (Fer-1), and the MDA content decreased after adding Fer-1, confirming that the production of MDA is due to the effect of ferroptosis (Figure 4D). Similarly, the content of LPO is also related to ferroptosis. When the C11-BODIPY probe changes from red to green, it indicates the production of LPO (Figure 4C). qRT-PCR and Western blot detected the expression of GPX4 protein related to ferroptosis (Figures 4E and 4F). The expression of GPX4 was down-regulated in cells after PTT and GMVD treatment, which also proved that PTT-triggered GMVD induced ferroptosis.

In vitro RT enhancement effect

Because gold can increase local energy deposition by emitting secondary electrons,[6] it can enhance the production of photoelectrons, Auger electrons and low-energy secondary electrons, directly damaging biological cells, and can increase the sensitivity of DNA to ionizing radiation.[49] It can also increase the sensitivity of DNA through oxidation stress.[50] Therefore, we further explored whether GMVD inherited the radiotherapy-sensitizing effect of gold element.

As shown in Figures 5A and 5D, GMVD alone did not significantly affect the proliferation rate of cells. HeLa cells are not sensitive to low-dose (≤4 Gy) X-rays. However, cells treated with GMVD showed significantly enhanced RT efficacy, which can reduce the cell colony formation rate by more than 20%, proving that GMVD is an excellent radiosensitizer. Under the same X-ray dose, GMVD's ability to inhibit cell proliferation is also better than CMNa, a common clinical radiotherapy sensitizer. This finding suggests that GMVD performs superior to clinically available sensitizers for tumor radiotherapy. In addition, cell migration assays showed that the migratory ability of cells treated with GMVD was significantly inhibited and the speed of wound healing was significantly reduced under a dose of 4 Gy of X-rays (Figures 4F and 4G).

In addition, ionizing radiation can cause DNA damage in tumor cells and then kill tumor cells through various mechanisms. Among them, affecting the cycle regulation of tumor cells, that is, reducing the G_2/M phase arrest of tumor cells, thereby affecting the repair of damaged DNA in tumor cells, and causing tumor cell death is one of the main mechanisms for its treatment of tumors.[51] The HeLa cells' cell cycle changes were evaluated by flow cytometry (Figures 5B, 5C, and 5E). It can be clearly observed that due to the DNA damage caused by
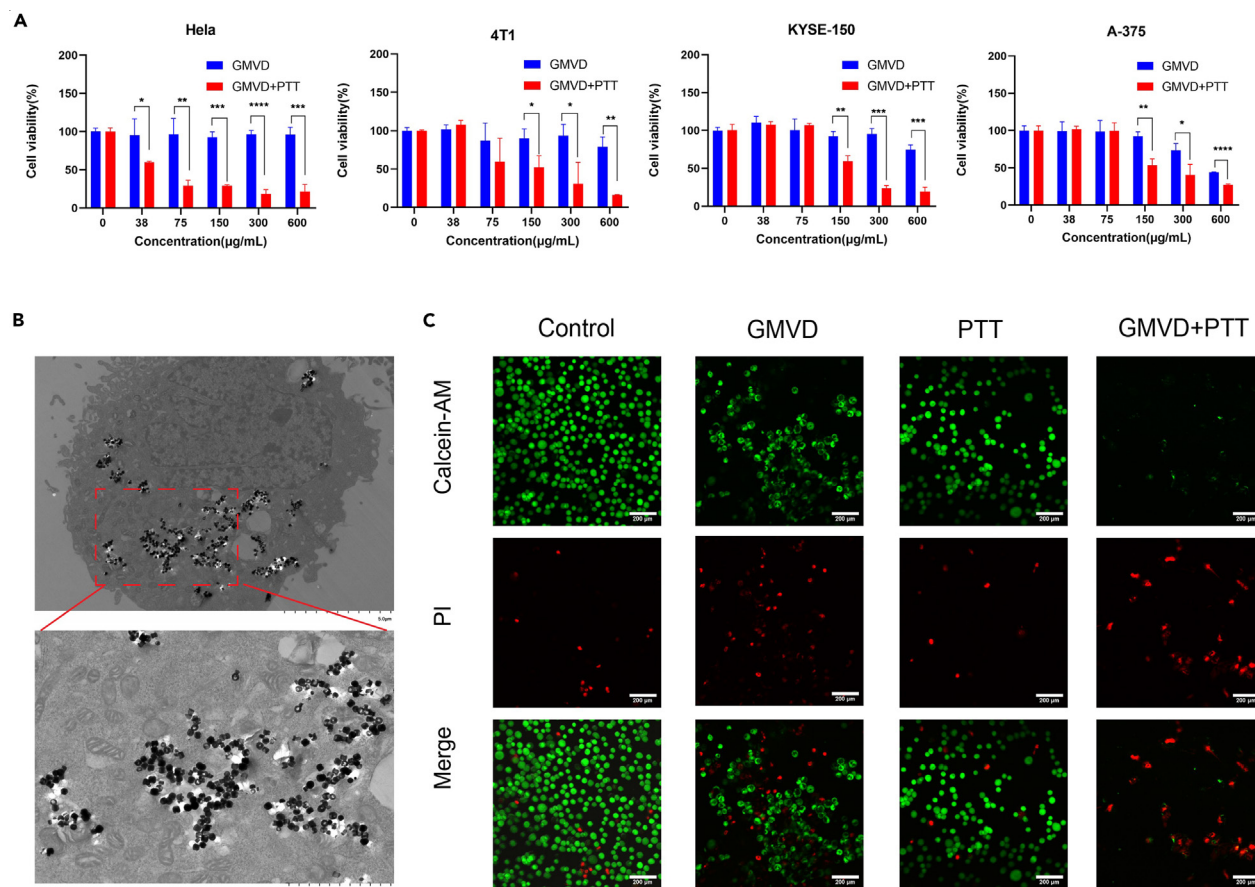
Figure 3. GMVD has photothermal therapeutic effects on various tumor cells

(A) Dark cytotoxicity and toxic effect of GMVD on HeLa, 4T1, KYSE-150 and A-375 cells. Values represent the means $\pm$ SD. (****$p < 0.0001$; ***$p < 0.001$; **$p < 0.01$*$p < 0.05$).

(B) Uptake of GMVD by cells, scale bar = 5.0/2.0 μm.

(C) Calcein-AM/PI live/dead cell staining on HeLa cells, scale bar = 200 μm.

the enhanced ionizing radiation as the concentration of GMVD increases, cells will initiate checkpoints immediately after DNA double-strand breaks to stop the cell cycle temporarily, checkpoints in G_1/S and S regulation prevents entry into S phase and shortens S phase, whereas G_2/M checkpoint regulation prevents entry into mitotic M phase and lengthens G_2 phase.

These results demonstrate that GMVD can enhance radiotherapy-induced decline in cell proliferation and migration and exacerbate ionizing radiation-induced DNA damage, providing a good radiosensitization effect.

In vitro and *in vivo* T$_2$-weighted MR imaging

Before *in vivo* experiments, we took the blood of mice for hemolysis assay to detect the biosafety of GMVD (Figure S11). The results showed that hemolysis did not occur even at a concentration of up to 1.2 mg/mL, which preliminary the demonstrated the proposed GMVD has good biocompatibility and that it could be safely used for *in vivo* experiments in mice.

In T$_2$-weighted (T$_2$W) MR Imaging, T$_2$ contrast agents selectively increase the transverse relaxation rate and lead to a darkening (negative contrast) in the region of interest. We first measured the *in vitro* T$_2$ MRI relaxation rate using a series of GMVD dispersions with a concentration of up to 0.8 mg/mL. The representative weighting images and the relaxation rates (r_2) are shown in Figures 6A and 6B, demonstrating a concentration-dependent negative enhancement. Notably, the transverse relaxation rates (R_2) for GMVD are 50.40 mM^{-1}S^{-1}, exhibiting an excellent contrasting capability for enhancing T$_2$ MRI.

Then, we studied the *in vivo* contrast enhancement by intravenous injection of GMVD (200 μL at 600 μg/mL) into 4T1-bearing mice. The T$_2$ signals in the tumor region exhibited a significant darkening starting from 2 h post-injection, which persisted until 24 h post-injection (Figures 6C and 6D). The T$_2$-MRI imaging achieved maximum contrast at 8 h post-injection, suggesting the most enormous amount of GMVD accumulation in the tumor area, providing the optimal time for treatment. Based on these results, we concluded that GMVD successfully accumulated and stayed at 4T1 tumor, and can act as an effective contrast agent for T$_2$-weighted MRI.
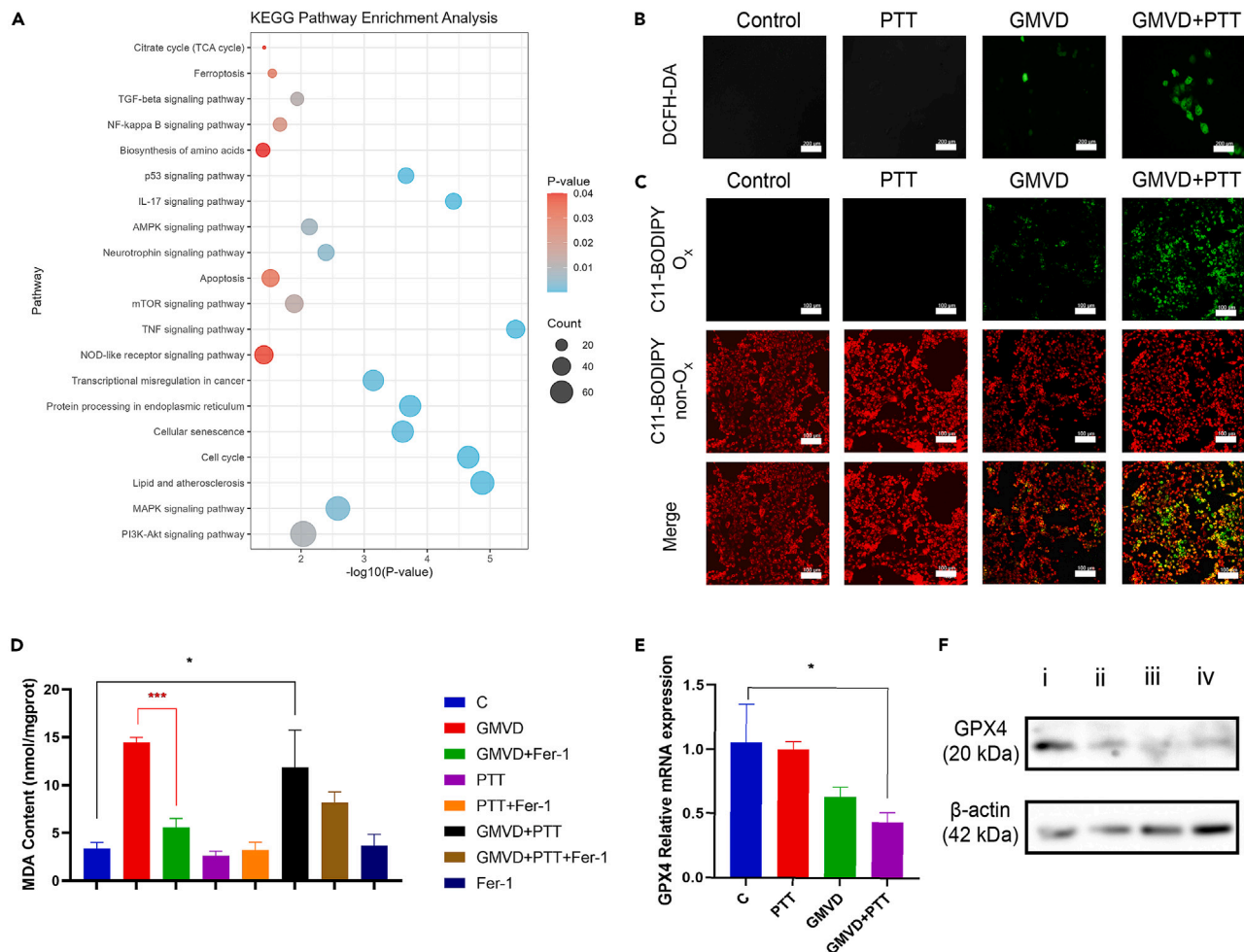
Figure 4. GMVD induces ferroptosis of tumor cells under the triggering of 808 nm laser

(A) Dot plot of KEGG enrichment analysis after RNA sequencing.

(B) Production of ROS after treatment with GMVD. Scale bar = 200 μm.

(C) Changes in LPO content after treatment with PTT and GMVD, green fluorescence represents LPO, and red fluorescence represents LP. Scale bar = 100 μm.

(D) Changes in MDA content after PTT, GMVD and Fer-1 treatment. Values represent the means $\pm$ SD. (*** $p < 0.001$; * $p < 0.05$).

(E) GPX4 expression measured by qRT-PCR. Values represent the means $\pm$ SD. (* $p < 0.05$).

(F) GPX4 expression measured by Western blot.

In vitro and *in vivo* photoacoustic imaging

Photoacoustic Imaging (PAI) is a biomedical imaging technology based on the photoacoustic effect that has developed rapidly in recent years. Gold nanoparticles are not only biocompatible and chemically inert, but also have unique surface plasmon resonance properties and high molar extinction coefficient, and thus are considered to be one of the most attractive PAI contrast agents.[52]

For *in vitro* PAI, the photoacoustic signal was significantly enhanced with increasing GMVD concentration (Figures 7A and 7C). After injecting GMVD into the tail vein of mice, the photoacoustic signal of the tumor site was tested. It was found that the photoacoustic signal reached the highest intensity at 8 h, and the photoacoustic signal returned to the level before injection after 24 h. This result is consistent with *in vivo* testing with MRI. Therefore, GMVD can significantly enhance the photoacoustic imaging signal in mice and reach the maximum cumulative concentration at the tumor site around 8 h (Figures 7B and 7D).

In vivo PTT/RT synergistic therapy in 4T1 tumor model

We then investigated the antitumor efficacy of GMVD-mediated PTT and/or RT in 4T1-bearing mice, which were randomly assigned to six treatment groups (3 mice per group): (1) saline as a control, (2) GMVD, (3) PTT+RT, (4) GMVD+PTT, (5) GMVD+RT, and (6) GMVD+PTT+RT. Imaging with a thermal infrared camera revealed that the surface temperature of tumors treated with GMVD and PTT reached 59°C within
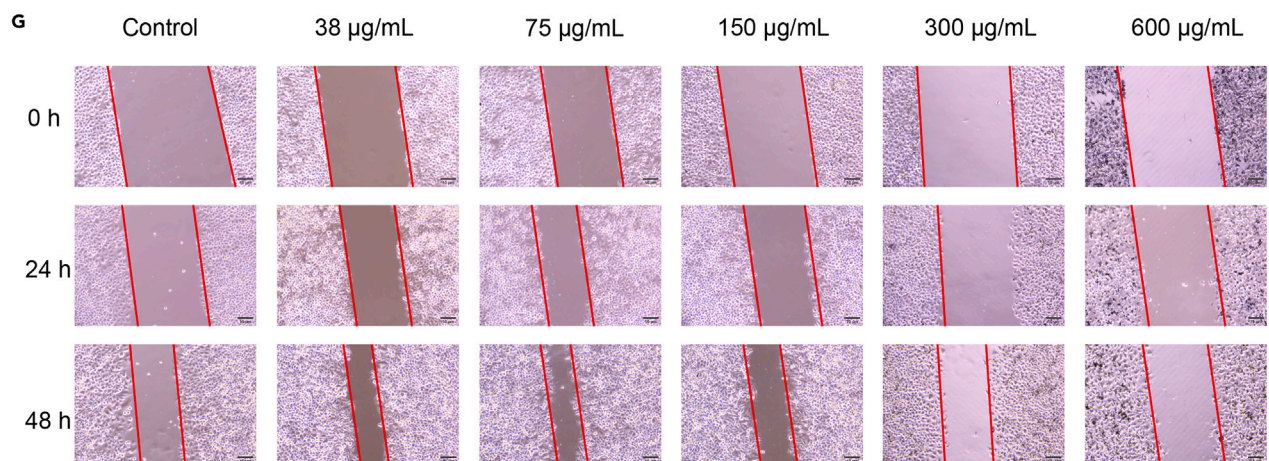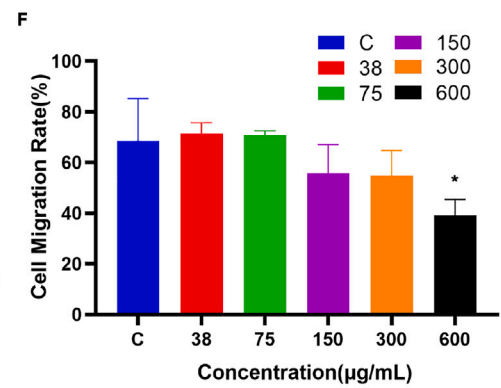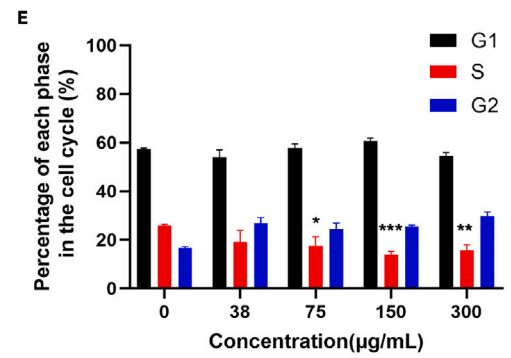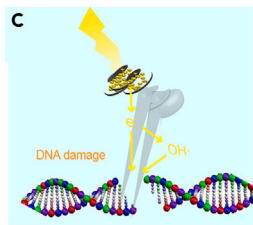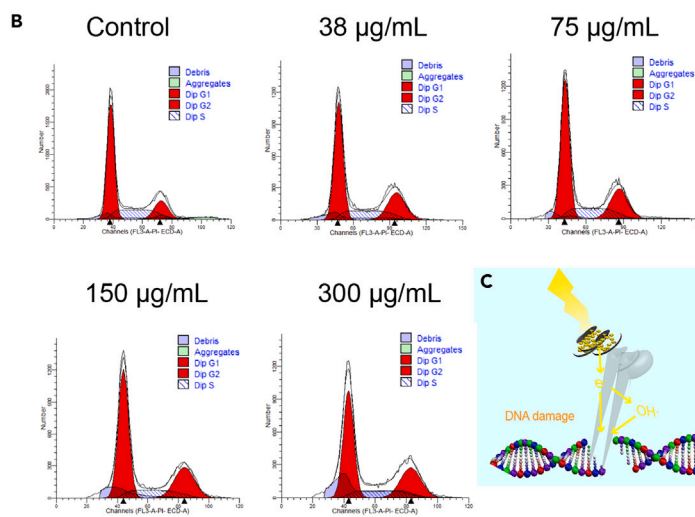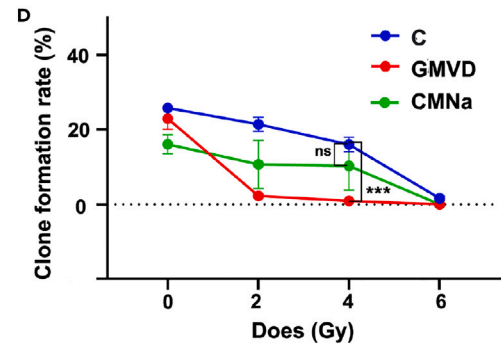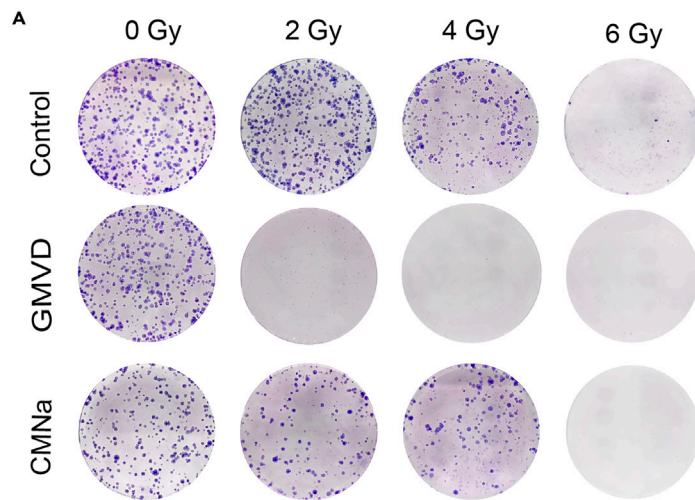
Figure 5. GMVD can enhance tumor radiotherapy sensitivity

(A and D) The clone formation and clone formation rate of GMVD and sodium glycididazole under different radiotherapy doses. Values represent the means $\pm$ SD. (***$p < 0.001$).

(B and E) Changes of HeLa cell cycle after treatment with different concentrations of GMVD. Values represent the means $\pm$ SD. (***$p < 0.001$; **$p < 0.01$; *$p < 0.05$).

(C) Schematic diagram of GMVD enhancing radiation-induced DNA damage.

(F and G) HeLa cell scratch test and cell migration rate after treatment with different concentrations of GMVD, scale bar = 10 μm. Values represent the means $\pm$ SD. (***$p < 0.001$; **$p < 0.01$; *$p < 0.05$).

10 min of laser irradiation, while the surface temperature of tumors treated with PTT only remained around 41°C at the end of 10 min laser irradiation (Figure 8A). Representative tumor and mice images are displayed 12 days after the initiation of treatment (Figures 8B and S12). As shown in Figure 8C, the tumors treated with GMVD+PTT+RT experienced an initial shrinkage during the first 4 days after treatment, while tumors in all other groups continued to grow, although at different rates. There was no significant change in body weight for the 4T1-bearing mice in all the groups (Figure 8D) for up to 12 days after the initiation of treatments. H&E staining showed that in the tumor site of the synergistic treatment group, the intercellular space was enlarged, the nucleus was obviously destroyed, and the staining decreased, indicating that the cell necrosis was obvious (Figure 8E). At the same time, after TUNEL staining, the collaborative treatment group showed stronger fluorescence, indicating that more tumor cells were undergoing apoptosis. In conclusion, we have demonstrated that GMVD is a promising agent to enhance PTT and RT for cancer therapy.

Furthermore, H&E staining of major organs, including the heart, liver, spleen, lung, and kidney, revealed no significant tissue damage or inflammatory lesions, further proving the biocompatibility of GMVD (Figure S13).
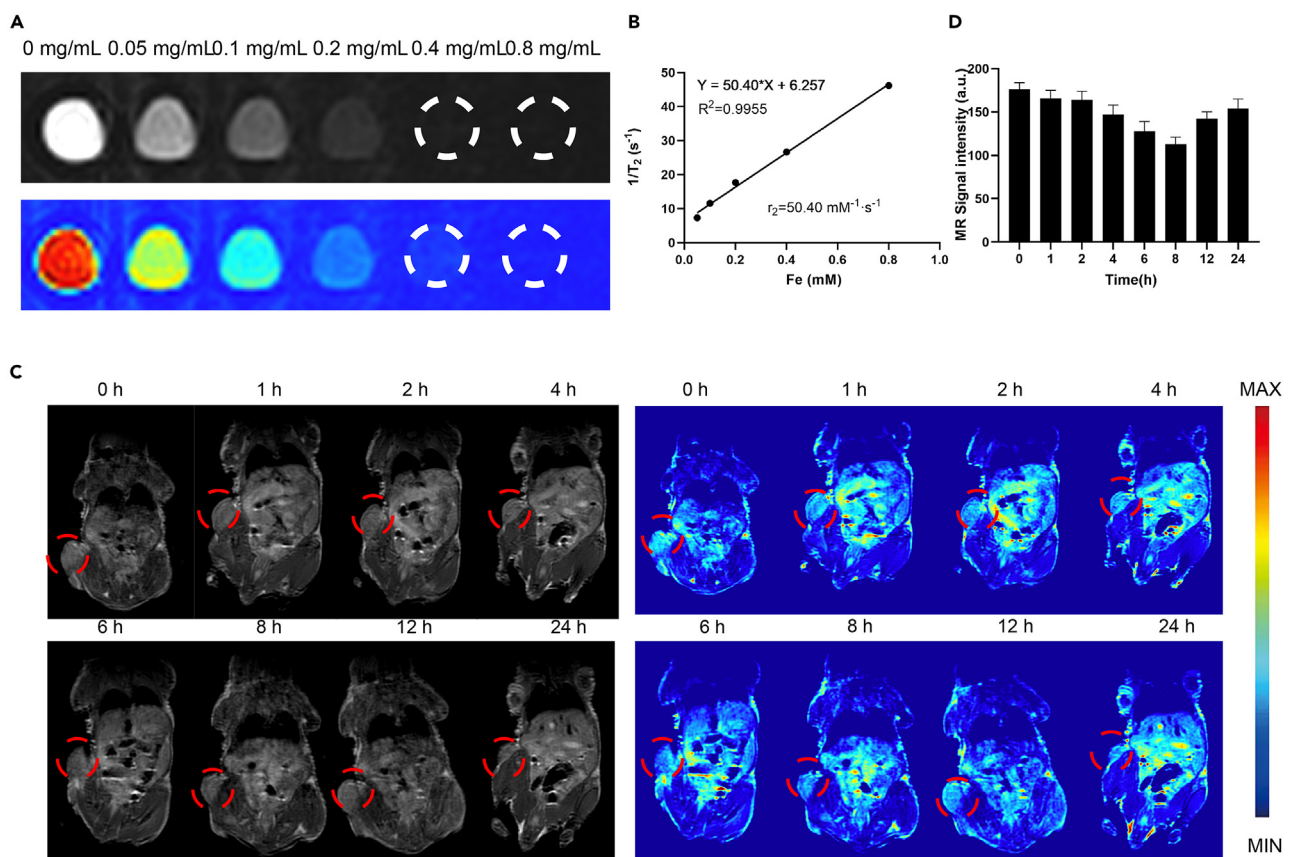
Figure 6. T$_2$-weighted MRI effects of GMVD *in vivo* and *in vitro*

(A) T$_2$-MR images of GMVD at different concentrations.

(B) the relaxation rates (r$_2$) of GMVD versus different concentrations of Fe^{3+}.

(C) *In vivo* T$_2$-MRI imaging of 4T1-bearing mice i.v. injected with 200 μL, 600 μg/mL GMVD acquired for up to 24 h after injecting the GMVD (red circles point to the tumor sites).

(D) Relative T$_2$ signal intensities of the tumor recorded at different time points post GMVD injection.
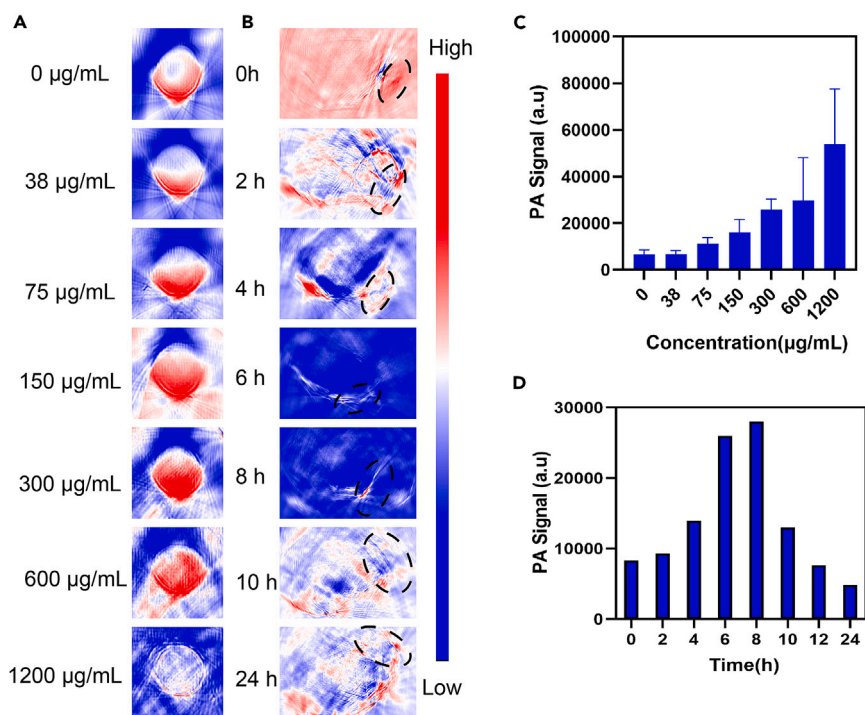
Figure 7. Photoacoustic imaging of GMVD *in vivo* and *in vitro*

(A) Photoacoustic imaging images of different concentrations of GMVD *in vitro*.

(B) Photoacoustic imaging images of the tumor site (circled) after tail vein injection of GMVD at different times.

(C) Signal intensity corresponding to *in vitro* photoacoustic imaging.

(D) Tumor site photoacoustic imaging at different times signal strength corresponding to acoustic imaging.

DISCUSSION

In the field of tumor therapy, the exclusive reliance on a single treatment method often encounters significant limitations. In recent years, the rapid development of nanotechnology has established a robust foundation for synergistic strategies in tumor therapy and opened up new avenues for multimodal diagnosis and treatment of tumors. Through the comprehensive utilization of nanomaterials with multiple therapeutic mechanisms and diagnostic functions, we are able to construct nanoplatforms integrating therapy and diagnosis, which points toward a novel pathway for the integration of tumor diagnosis and treatment. MNPs have gradually become a hot topic of research due to their unique superparamagnetism, excellent biocompatibility and targeting. Under the action of a magnetic field, MNPs exhibit excellent magnetic sensitivity, and their targeted drug loading, magnetic resonance imaging and magnetothermal effect provide an effective way to treat tumors.

Although MNPs have been demonstrated to possess considerable potential for tumor thermotherapy, the lack of photothermal or magnetothermal conversion efficiency currently limits their wide clinical application. Consequently, the development of MNPs with higher SAR to reduce the clinical dosage of conversion agents represents a crucial step in advancing the clinical translation of tumor thermotherapy. In this study, the objective was to develop magnetic iron oxide NPs with enhanced conversion efficiency for the efficient thermotherapy of tumors. Additionally, the T_2 relaxation time-shortening effect of magnetic iron oxide NPs was exploited for MR imaging of tumors. Furthermore, the combination of Au, which can absorb NIR light, enhanced the photothermal conversion performance of magnetic iron oxide NPs, while also endowing them with the ability to perform PA imaging.

In conclusion, we successfully designed and synthesized GMVD as a multifunctional drug integrating MRI/PAI-guided diagnosis and dual-thermal/enhanced RT synergistic therapy. The unique ring structure gives it excellent magnetothermal ability (SAR = 1747.48 W/g), and GMVD exhibits a wide range of NIR absorbance and excellent photothermal ability (η = 42.2%). In addition, with the help of NIR laser irradiation, GMVD showed efficient ROS generation and DNA damage, successfully inducing ferroptosis. Based on *in vitro* and *in vivo* observations, GMVD exhibits excellent anti-tumor ability under low laser power and appropriate X-ray irradiation, which may be attributed to Fenton reaction and ferroptosis. GMVD demonstrated satisfactory biosafety in multiple cell and mouse models with no observable toxicity. Notably, GMVD significantly enhanced T_2-weighted MR and photoacoustic contrast for *in vitro* and *in vivo* imaging. Therefore, the prepared GMVD shows great potential as a nanotherapeutic agent for MRI/PAI-guided PTT/magnetothermal/enhanced RT synergistic therapy in future clinical trials.
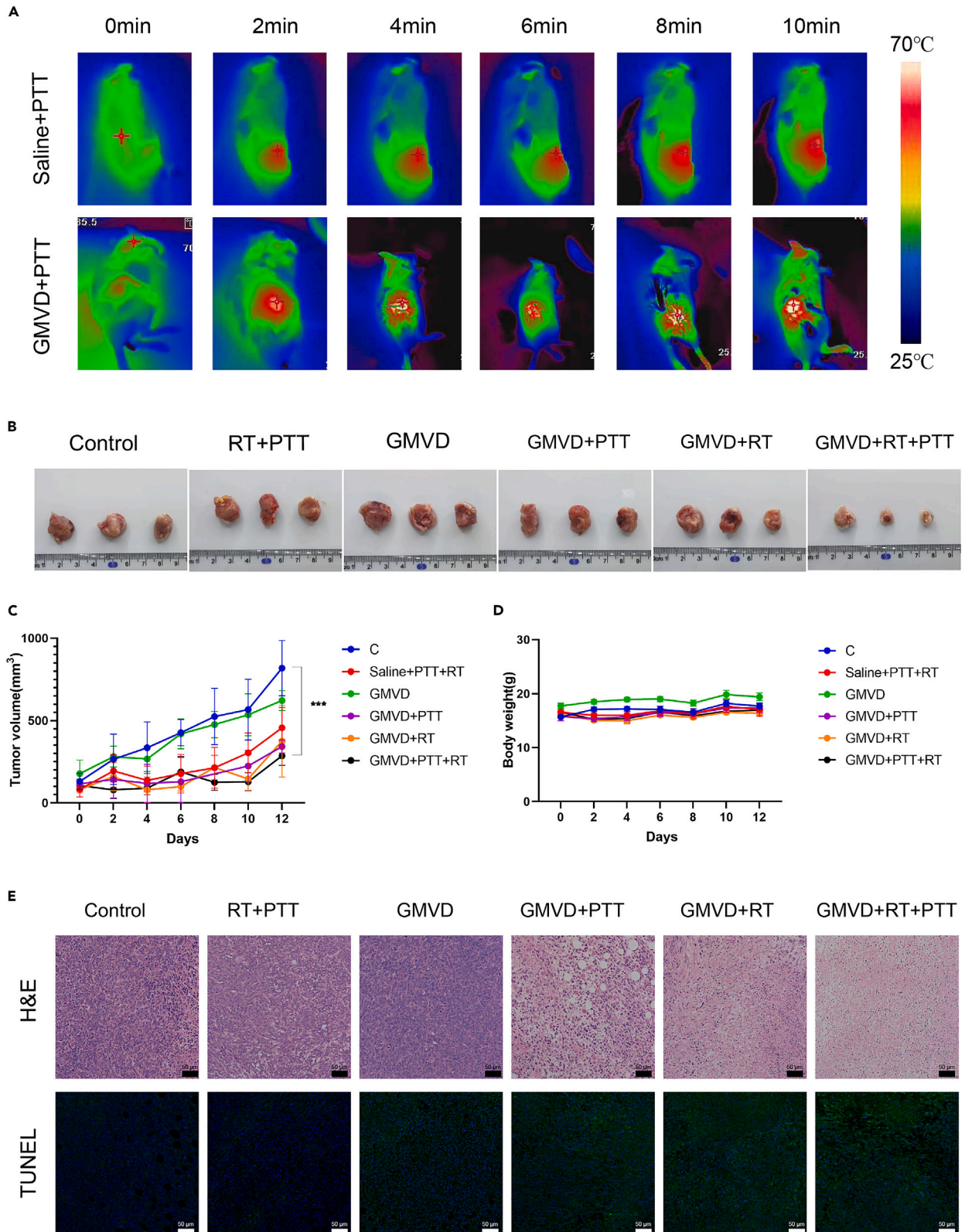
Figure 8. GMVD synergizes with PTT and RT *in vivo* to induce tumor ablation

(A) Representative infrared thermal images of tumor-bearing mice injected with saline or GMVD during laser irradiation. The 808-nm laser was applied 8 h after injection at a power density of 1.6 W/cm^2 for 10 min.

(B) Representative photographs of excised tumors after the initiation of treatments.

(C) Relative tumor growth curves after the initiation of treatments. Data are presented as mean $\pm$ standard error of mean (SEM). Values represent the means $\pm$ SD. (***$p < 0.001$).

(D) Body weight of mice in each treatment group ($n = 3$).

(E) Representative hematoxylin-eosin and TUNEL staining of tumor sections of each treatment group. Scale bar = 50 μm.

Limitations of the study

Although GMVD exhibits good magnetocaloric and photothermal effects, its aggregation problem has not been well solved. At present, the synthesis methods of magnetic iron oxide NPs mainly include coprecipitation, hydrothermal, high-temperature thermal decomposition, etc. Although these mature preparation methods can synthesize MNPs with good uniformity and activity, the reaction process is affected by conditions such as solution pH, temperature, and reaction time, and aggregation is prone to occur. The shape and size of the particles are also difficult to control, which affects their performance in tumor treatment. Therefore, improving the stability and dispersibility of magnetic iron oxide NPs is the key to its successful application. In order to maintain the specific properties of magnetic iron oxide NPs, modification is one of the common methods. The modification of magnetic nanomaterials is mainly divided into inorganic material modification and organic modification. Inorganic materials mainly include silica, gold, carbon, etc. The modification of magnetic iron oxide NPs with organic polymers has gradually become the most widely used method in biomedicine, such as adding appropriate organic stabilizers during the preparation process to control the distribution of particle size to obtain magnetic iron oxide NPs with uniform size. The organic materials used mainly include polyethylene glycol (PEG), polyvinyl alcohol (PVA), chitosan and some macromolecular proteins. In the future, we will also consider using reasonable methods to modify GMVD to make it have superior dispersibility and better fit future clinical transformation applications.

In addition, the article only preliminarily explored the phenomenon of photothermal-triggered GMVD-induced ferroptosis, and did not conduct in-depth research on the mechanism of this phenomenon. It has been reported that in the presence of photothermal conversion materials, temperature increase can accelerate the Fenton reaction kinetics.[53] On the one hand, light irradiation promotes the generation of ROS of iron therapeutics through direct electron transfer and light-enhanced Fenton reaction, while the photothermal effect can improve the generation of ROS.[54] On the other hand, hyperthermia affects intracellular enzyme activity and destroys the inherent resistance of cancer cells (e.g., ferroptosis-related proteins, unstable iron pools, and respiratory enzymes), resulting in an ideal anti-tumor therapeutic effect.[55] GMVD mediates the process of ferroptosis mainly by generating Fe^{2+} ions and thus catalyzing the Fenton-like reaction.[56] The increase in temperature during PTT can accelerate the Fenton-like reaction and enhance the tumor killing ability of ferroptosis.[57] We verified these two hypotheses and found that under 808 nm laser triggering, GMVD significantly produced ROS and produced more Fe^{2+} ions than MVD. Due to time and space constraints, we were unable to further verify the mechanism of GMVD-triggered ferroptosis. We will further explore related issues in subsequent experimental studies.

RESOURCE AVAILABILITY

Lead contact

Further information and requests for resources and reagents should be directed to and will be fulfilled by the lead contact, Z.J. (jizhenyu@zzu.edu.cn).

Materials availability

This study did not generate new unique reagents.

Data and code availability

- All data reported in this paper will be shared by the lead contact upon request.
- This paper does not report original code.
- Any additional information required to re-analyze the data reported in this paper is available from the lead contact upon request.

AUTHOR CONTRIBUTIONS

S.G.: Investigation, Writing-original draft, Methodology. M.C.: Project administration. Y.Y.: Validation. X.P.: Software, Visualization. Y.S.: Formal analysis. Y.Z.: Data curation. D.F.: Supervision. J.B.: Writing-review and editing. Z.J.: Conceptualization, Resources.

DECLARATION OF INTERESTS

There are no conflicts to declare.

STAR★METHODS

Detailed methods are provided in the online version of this paper and include the following:

SUPPLEMENTAL INFORMATION

Supplemental information can be found online at https://doi.org/10.1016/j.isci.2024.110533.

REFERENCES

1. McGuire, S. (2016). World Cancer Report 2014. Geneva, Switzerland: World Health Organization, International Agency for Research on Cancer, WHO Press, 2015. Adv. Nutr. 7, 418–419. https://doi.org/10.3945/an.116.012211.

2. Kwizera, E.A., Stewart, S., Mahmud, M.M., and He, X. (2022). Magnetic Nanoparticle-Mediated Heating for Biomedical Applications. J. Heat Transfer 144, 30801. https://doi.org/10.1115/1.4053007.

3. Wei, G., Wang, Y., Yang, G., Wang, Y., and Ju, R. (2021). Recent progress in nanomedicine for enhanced cancer chemotherapy. Theranostics 11, 6370–6392. https://doi.org/10.7150/thno.57828.

4. Duan, S., Hu, Y., Zhao, Y., Tang, K., Zhang, Z., Liu, Z., Wang, Y., Guo, H., Miao, Y., Du, H., et al. (2023). Nanomaterials for photothermal cancer therapy. RSC Adv. 13, 14443–14460. https://doi.org/10.1039/d3ra02620e.

5. Olivares-Urbano, M.A., Griñán-Lisón, C., Marchal, J.A., and Núñez, M.I. (2020). CSC Radioresistance: A Therapeutic Challenge to Improve Radiotherapy Effectiveness in Cancer. Cells 9, 1651. https://doi.org/10.3390/cells9071651.

6. Chen, Y., Yang, J., Fu, S., and Wu, J. (2020). Gold Nanoparticles as Radiosensitizers in Cancer Radiotherapy. Int. J. Nanomed. 15, 9407–9430. https://doi.org/10.2147/ijn.S272902.

7. Wen, S., Ovais, M., Li, X., Ren, J., Liu, T., Wang, Z., Cai, R., and Chen, C. (2022). Tailoring bismuth-based nanoparticles for enhanced radiosensitivity in cancer therapy. Nanoscale 14, 8245–8254. https://doi.org/10.1039/d2nr01500e.

8. Gai, S., Li, C., Yang, P., and Lin, J. (2014). Recent progress in rare earth micro/nanocrystals: soft chemical synthesis, luminescent properties, and biomedical applications. Chem. Rev. 114, 2343–2389. https://doi.org/10.1021/cr4001594.

9. Shen, Z., Liu, T., Li, Y., Lau, J., Yang, Z., Fan, W., Zhou, Z., Shi, C., Ke, C., Bregadze, V.I., et al. (2018). Fenton-Reaction-Acceleratable Magnetic Nanoparticles for Ferroptosis Therapy of Orthotopic Brain Tumors. ACS Nano 12, 11355–11365. https://doi.org/10.1021/acsnano.8b06201.

10. Espinosa, A., Di Corato, R., Kolosnjaj-Tabi, J., Flaud, P., Pellegrino, T., and Wilhelm, C. (2016). Duality of Iron Oxide Nanoparticles in Cancer Therapy: Amplification of Heating Efficiency by Magnetic Hyperthermia and Photothermal Bimodal Treatment. ACS Nano 10, 2436–2446. https://doi.org/10.1021/acsnano.5b07249.

11. Shakeri-Zadeh, A., Khoei, S., Khoee, S., Sharifi, A.M., and Shiran, M.-B. (2015). Combination of ultrasound and newly synthesized magnetic nanocapsules affects the temperature profile of CT26 tumors in BALB/c mice. J. Med. Ultrason. 42, 9–16. https://doi.org/10.1007/s10396-014-0558-4.

12. Yan, B., Wang, S., Liu, C., Wen, N., Li, H., Zhang, Y., Wang, H., Xi, Z., Lv, Y., Fan, H., and Liu, X. (2022). Engineering magnetic nano-manipulators for boosting cancer immunotherapy. J. Nanobiotechnol. 20, 547. https://doi.org/10.1186/s12951-022-01760-8.

13. Amin, M., Huang, W., Seynhaeve, A.L.B., and Ten Hagen, T.L.M. (2020). Hyperthermia and Temperature-Sensitive Nanomaterials for Spatiotemporal Drug Delivery to Solid Tumors. Pharmaceutics 12, 1007. https://doi.org/10.3390/pharmaceutics12111007.

14. Liu, X., Zhang, Y., Wang, Y., Zhu, W., Li, G., Ma, X., Zhang, Y., Chen, S., Tiwari, S., Shi, K., et al. (2020). Comprehensive understanding of magnetic hyperthermia for improving antitumor therapeutic efficacy. Theranostics 10, 3793–3815. https://doi.org/10.7150/thno.40805.

15. Lv, R., Jiang, X., Yang, F., Wang, Y., Feng, M., Liu, J., and Tian, J. (2019). Degradable magnetic-response photoacoustic/up-conversion luminescence imaging-guided photodynamic/photothermal antitumor therapy. Biomater. Sci. 7, 4558–4567. https://doi.org/10.1039/C9BM00853E.

16. Majeed, J., Pradhan, L., Ningthoujam, R.S., Vatsa, R.K., Bahadur, D., and Tyagi, A.K. (2014). Enhanced specific absorption rate in silanol functionalized Fe_3O_4 core–shell nanoparticles: Study of Fe leaching in Fe3O4 and hyperthermia in L929 and HeLa cells. Colloids Surf. B Biointerfaces 122, 396–403. https://doi.org/10.1016/j.colsurfb.2014.07.019.

17. Xie, J., Zhang, Y., Yan, C., Song, L., Wen, S., Zang, F., Chen, G., Ding, Q., Yan, C., and Gu, N. (2014). High-performance PEGylated Mn–Zn ferrite nanocrystals as a passive-targeted agent for magnetically induced cancer theranostics. Biomaterials 35, 9126–9136. https://doi.org/10.1016/j.biomaterials.2014.07.019.

18. Liu, X.L., Ng, C.T., Chandrasekharan, P., Yang, H.T., Zhao, L.Y., Peng, E., Lv, Y.B., Xiao, W., Fang, J., Yi, J.B., et al. (2016). Synthesis of Ferromagnetic Fe0.6Mn0.4O Nanoflowers as a New Class of Magnetic Theranostic Platform for In Vivo T1-T2 Dual-Mode Magnetic Resonance Imaging and Magnetic Hyperthermia Therapy. Adv. Healthc. Mater. 5, 2092–2104. https://doi.org/10.1002/adhm.201600357.

19. Castellanos-Rubio, I., Munshi, R., Qin, Y., Eason, D.B., Orue, I., Insausti, M., and Pralle, A. (2018). Multilayered inorganic-organic microdisks as ideal carriers for high magnetothermal actuation: assembling ferrimagnetic nanoparticles devoid of dipolar interactions. Nanoscale 10, 21879–21892. https://doi.org/10.1039/c8nr03869d.

20. Li, J., Zu, X., Liang, G., Zhang, K., Liu, Y., Li, K., Luo, Z., and Cai, K. (2018). Octopod PtCu Nanoframe for Dual-Modal Imaging-Guided Synergistic Photothermal Radiotherapy. Theranostics 8, 1042–1058. https://doi.org/10.7150/thno.22557.

21. Liu, Y., Crawford, B.M., and Vo-Dinh, T. (2018). Gold nanoparticles-mediated photothermal therapy and immunotherapy. Immunotherapy 10, 1175–1188. https://doi.org/10.2217/imt-2018-0029.

22. Lv, R., Raab, M., Wang, Y., Tian, J., Lin, J., and Prasad, P.N. (2022). Nanochemistry advancing photon conversion in rare-earth nanostructures for theranostics. Coord. Chem. Rev. 460, 214486. https://doi.org/10.1016/j.ccr.2022.214486.

23. Zhao, L., Zhang, X., Wang, X., Guan, X., Zhang, W., and Ma, J. (2021). Recent advances in selective photothermal therapy of tumor. J. Nanobiotechnol. 19, 335. https://doi.org/10.1186/s12951-021-01080-3.

24. Zheng, Z., Jia, Z., Qin, Y., Dai, R., Chen, X., Ma, Y., Xie, X., and Zhang, R. (2021). All-in-One Zeolite-Carbon-Based Nanotheranostics with Adjustable NIR-II Window Photoacoustic/ Fluorescence Imaging Performance for Precise NIR-II Photothermal-Synergized Catalytic Antitumor Therapy. Small 17, e2103252. https://doi.org/10.1002/smll.202103252.

25. Li, Z., Chen, Y., Yang, Y., Yu, Y., Zhang, Y., Zhu, D., Yu, X., Ouyang, X., Xie, Z., Zhao, Y., and Li, L. (2019). Recent Advances in Nanomaterials-Based Chemo-Photothermal Combination Therapy for Improving Cancer Treatment. Front. Bioeng. Biotechnol. 7, 293. https://doi.org/10.3389/fbioe.2019.00293.

26. Kim, H., Chung, K., Lee, S., Kim, D.H., and Lee, H. (2016). Near-infrared light-responsive nanomaterials for cancer theranostics. Wiley interdisciplinary reviews. Nanomed. Nanobiotechnol. 8, 23–45. https://doi.org/10.1002/wnan.1347.

27. Pei, Z., Lei, H., and Cheng, L. (2023). Bioactive inorganic nanomaterials for cancer theranostics. Chem. Soc. Rev. 52, 2031–2081. https://doi.org/10.1039/d2cs00352j.

28. Rajana, N., Mounika, A., Chary, P.S., Bhavana, V., Urati, A., Khatri, D., Singh, S.B., and Mehra, N.K. (2022). Multifunctional hybrid nanoparticles in diagnosis and therapy of breast cancer. J. Control. Release 352, 1024–1047. https://doi.org/10.1016/j.jconrel.2022.11.009.

29. Cristofolini, T., Dalmina, M., Sierra, J.A., Silva, A.H., Pasa, A.A., Pittella, F., and Creczynski-Pasa, T.B. (2020). Multifunctional hybrid nanoparticles as magnetic delivery systems for siRNA targeting the HER2 gene in breast cancer cells. Mat. Sci. Eng. C. Mat. Biol. Appl. 109, 110555. https://doi.org/10.1016/j.msec.2019.110555.

30. de la Encarnación, C., Jimenez de Aberasturi, D., and Liz-Marzán, L.M. (2022). Multifunctional plasmonic-magnetic nanoparticles for bioimaging and hyperthermia. Adv. Drug Deliv. Rev. 189, 114484. https://doi.org/10.1016/j.addr.2022.114484.

31. Liu, X.-L., Yang, Y., Wu, J.-P., Zhang, Y.-F., Fan, H.-M., and Ding, J. (2015). Novel magnetic vortex nanorings/nanodiscs: Synthesis and theranostic applications. Chinese Phys. B 24, 127505.

32. Kim, J.E., Choi, J.H., Colas, M., Kim, D.H., and Lee, H. (2016). Gold-based hybrid nanomaterials for biosensing and molecular diagnostic applications. Biosens. Bioelectron. 80, 543–559.

33. Tian, Y., Qiang, S., and Wang, L. (2019). Gold nanomaterials for imaging-guided near-infrared in vivo cancer therapy. Front. Bioeng. Biotechnol. 7, 398.

34. Eyvazzadeh, N., Shakeri-Zadeh, A., Fekrazad, R., Amini, E., Ghaznavi, H., and Kamran Kamrava, S. (2017). Gold-coated magnetic nanoparticle as a nanotheranostic agent for magnetic resonance imaging and photothermal therapy of cancer. Lasers Med. Sci. 32, 1469–1477. https://doi.org/10.1007/s10103-017-2267-x.

35. Jia, C.J., Sun, L.D., Luo, F., Han, X.D., Heyderman, L.J., Yan, Z.G., Yan, C.H., Zheng, K., Zhang, Z., Takano, M., et al. (2008). Large-scale synthesis of single-crystalline iron oxide magnetic nanorings. J. Am. Chem. Soc. 130, 16968–16977. https://doi.org/10.1021/ja805152t.

36. Hui, W., Shi, F., Yan, K., Peng, M., Cheng, X., Luo, Y., Chen, X., Roy, V.A.L., Cui, Y., and Wang, Z. (2012). Fe3O4/Au/Fe3O4 nanoflowers exhibiting tunable saturation magnetization and enhanced bioconjugation. Nanoscale 4, 747–751. https://doi.org/10.1039/C2NR11489E.

37. Chen, J., Liu, X., Liu, Z., Ma, J., Han, J., Sun, Y., Liang, J., Han, H., Zhao, J., Wang, B., et al. (2024). Ultrasensitive SERS biosensor for synchronous detection of Escherichia coli O157:H7 and Pseudomonas aeruginosa via Cecropin 1-functionalized magnetic tags-based lateral flow assay. Sens. Actuators B Chem. 409, 135598. https://doi.org/10.1016/j.snb.2024.135598.

38. Levin, C.S., Hofmann, C., Ali, T.A., Kelly, A.T., Morosan, E., Nordlander, P., Whitmire, K.H., and Halas, N.J. (2009). Magnetic−Plasmonic Core−Shell Nanoparticles. ACS Nano 3, 1379–1388. https://doi.org/10.1021/nn900118a.

39. Sundar, D.S., Antoniraj, M.G., Kumar, C.S., Mohapatra, S.S., Houreld, N.N., and Ruckmani, K. (2016). Recent Trends of Biocompatible and Biodegradable Nanoparticles in Drug Delivery: A Review. Curr. Med. Chem. 23, 3730–3751. https://doi.org/10.2174/0929867323666160607103854.

40. Gao, F., Xie, W., Miao, Y., Wang, D., Guo, Z., Ghosal, A., Li, Y., Wei, Y., Feng, S.S., Zhao, L., and Fan, H.M. (2019). Magnetic Hydrogel with Optimally Adaptive Functions for Breast Cancer Recurrence Prevention. Adv. Healthc. Mater. 8, e1900203. https://doi.org/10.1002/adhm.201900203.

41. Bao, J., Guo, S., Zu, X., Zhuang, Y., Fan, D., Zhang, Y., Shi, Y., Pang, X., Ji, Z., and Cheng, J. (2022). Magnetic vortex nanoring coated with gadolinium oxide for highly enhanced T(1)-T(2) dual-modality magnetic resonance imaging-guided magnetic hyperthermia cancer ablation. Biomed. Pharmaco. 150, 112926. https://doi.org/10.1016/j.biopha.2022.112926.

42. Jiang, X., Stockwell, B.R., and Conrad, M. (2021). Ferroptosis: mechanisms, biology and role in disease. Nat. Rev. Mol. Cell Biol. 22, 266–282. https://doi.org/10.1038/s41580-020-00324-8.

43. Xie, S., Sun, W., Zhang, C., Dong, B., Yang, J., Hou, M., Xiong, L., Cai, B., Liu, X., and Xue, W. (2021). Metabolic Control by Heat Stress Determining Cell Fate to Ferroptosis for Effective Cancer Therapy. ACS Nano 15, 7179–7194. https://doi.org/10.1021/acsnano.1c00380.

44. Tang, D., Chen, X., Kang, R., and Kroemer, G. (2021). Ferroptosis: molecular mechanisms and health implications. Cell Res. 31, 107–125. https://doi.org/10.1038/s41422-020-00441-1.

45. Battaglia, A.M., Chirillo, R., Aversa, I., Sacco, A., Costanzo, F., and Biamonte, F. (2020). Ferroptosis and Cancer: Mitochondria Meet the "Iron Maiden" Cell Death. Cells 9, 1505. https://doi.org/10.3390/cells9061505.

46. Lei, G., Zhuang, L., and Gan, B. (2022). Targeting ferroptosis as a vulnerability in cancer. Nat. Rev. Cancer 22, 381–396. https://doi.org/10.1038/s41568-022-00459-0.

47. Li, J., Cao, F., Yin, H.L., Huang, Z.J., Lin, Z.T., Mao, N., Sun, B., and Wang, G. (2020). Ferroptosis: past, present and future. Cell Death Dis. 11, 88. https://doi.org/10.1038/s41419-020-2298-2.

48. Chen, X., Li, J., Kang, R., Klionsky, D.J., and Tang, D. (2021). Ferroptosis: machinery and regulation. Autophagy 17, 2054–2081. https://doi.org/10.1080/15548627.2020.1810918.

49. Haume, K., Rosa, S., Grellet, S., Śmiałek, M.A., Butterworth, K.T., Solov'yov, A.V., Prise, K.M., Golding, J., and Mason, N.J. (2016). Gold nanoparticles for cancer radiotherapy: a review. Cancer Nanotechnol. 7, 8. https://doi.org/10.1186/s12645-016-0021-x.

50. Laprise-Pelletier, M., Simão, T., and Fortin, M.A. (2018). Gold Nanoparticles in Radiotherapy and Recent Progress in Nanobrachytherapy. Adv. Healthc. Mater. 7, e1701460. https://doi.org/10.1002/adhm.201701460.

51. Remigio, A.S. (2021). In silico simulation of the effect of hypoxia on MCF-7 cell cycle kinetics under fractionated radiotherapy. J. Biol. Phys. 47, 301–321. https://doi.org/10.1007/s10867-021-09580-x.

52. Cai, K., Zhang, W., Foda, M.F., Li, X., Zhang, J., Zhong, Y., Liang, H., Li, H., Han, H., and Zhai, T. (2020). Miniature Hollow Gold Nanorods with Enhanced Effect for In Vivo Photoacoustic Imaging in the NIR-II Window. Small 16, e2002748. https://doi.org/10.1002/smll.202002748.

53. He, S., Jiang, Y., Li, J., and Pu, K. (2020). Semiconducting Polycomplex Nanoparticles for Photothermal Ferrotherapy of Cancer. Angew. Chem. Int. Ed. Engl. 59, 10633–10638. https://doi.org/10.1002/anie.202003004.

54. Wei, R., Fu, G., Li, Z., Liu, Y., Qi, L., Liu, K., Zhao, Z., and Xue, M. (2024). Au-Fe3O4 Janus nanoparticles for imaging-guided near infrared-enhanced ferroptosis therapy in triple negative breast cancer. J. Colloid Interface Sci. 663, 644–655. https://doi.org/10.1016/j.jcis.2024.02.201.

55. Qin, W., Huang, J., Yang, C., Yue, Q., Chen, S., Wang, M., Gao, S., Zhou, X., Yang, X., and Zhang, Y. (2023). Protease-Activatable Nanozyme with Photoacoustic and Tumor-Enhanced Magnetic Resonance Imaging for Photothermal Ferroptosis Cancer Therapy. Adv. Funct. Mater. 33, 2209748. https://doi.org/10.1002/adfm.202209748.

56. Zeng, F., Tang, L., Zhang, Q., Shi, C., Huang, Z., Nijiati, S., Chen, X., and Zhou, Z. (2022). Coordinating the Mechanisms of Action of Ferroptosis and the Photothermal Effect for Cancer Theranostics. Angew. Chem. Int. Ed.

Engl. *61*, e202112925. https://doi.org/10.
1002/anie.202112925.

57. Yuan, H., Xia, P., Sun, X., Ma, J., Xu, X., Fu, C.,
Zhou, H., Guan, Y., Li, Z., Zhao, S., et al. (2022).
Photothermal Nanozymatic Nanoparticles
Induce Ferroptosis and Apoptosis through
Tumor Microenvironment Manipulation for
Cancer Therapy. Small *18*, e2202161. https://
doi.org/10.1002/smll.202202161.

58. Jia, C.-J., Sun, L.-D., Luo, F., Han, X.-D.,
Heyderman, L.J., Yan, Z.-G., Yan, C.-H.,
Zheng, K., Zhang, Z., Takano, M., et al. (2008).

Large-Scale Synthesis of Single-Crystalline
Iron Oxide Magnetic Nanorings. J. Am.
Chem. Soc. *130*, 16968–16977. https://doi.
org/10.1021/ja805152t.

59. Brown, K.R., Walter, D.G., and Natan, M.J.
(2000). Seeding of Colloidal Au
Nanoparticle Solutions. 2. Improved
Control of Particle Size and Shape. Chem.
Mater. *12*, 306–313. https://doi.org/10.
1021/cm980065p.

60. Goon, I.Y., Lai, L.M.H., Lim, M., Munroe, P.,
Gooding, J.J., and Amal, R. (2009).

Fabrication and Dispersion of Gold-Shell-
Protected Magnetite Nanoparticles:
Systematic Control Using Polyethyleneimine.
Chem. Mater. *21*, 673–681. https://doi.org/
10.1021/cm8025329.

61. Bonvin, D., Alexander, D.T., Millán, A., Piñol,
R., Sanz, B., Goya, G.F., Martínez, A.,
Bastiaansen, J.A., Stuber, M., Schenk, K.J.,
et al. (2017). Tuning properties of iron oxide
nanoparticles in aqueous synthesis without
ligands to improve MRI relaxivity and SAR.
Nanomaterials *7*, 225.

STAR★METHODS

KEY RESOURCES TABLE

REAGENT or RESOURCE	SOURCE	IDENTIFIER
Antibodies		
GPX4	Proteintech	RRID: 67763-1-Ig
β-actin	Proteintech	RRID: 66009-1-Ig
Chemicals, peptides, and recombinant proteins		
Trizol	TaKaRa	Cat#9108
RPMI Medium 1640	Solarbio	Cat#31800
Trypsin-EDTA solution, 0.25% (without phenol red)	Solarbio	Cat# T1300
Fetal bovine serum (FBS)	Cell-Box	Cat# AUS-01S-02
4% paraformaldehyde	Solarbio	Cat#P1110
Critical commercial assays		
Cell counting kit-8 (CCK-8)	Dojindo	Cat#CK04
Calcein-AM/PI Double Stain Kit	Dojindo	Cat#C542
Lipid Peroxidation Probe -BDP 581/591 C11	Dojindo	Cat#L267
FerroOrange	Dojindo	Cat# F374
Cell Malondialdehyde (MDA) assay kit (Colorimetric method)	Nanjing Jiancheng	Cat# A003-4-1
Reactive Oxygen Species Assay Kit	KeyGen	Cat# KGA7308-100
cell cycle Assay Kit	KeyGen	Cat# KGA9101-100
SYBR® Green PCR Master Mix	TaKaRa	Cat# RR420A
PrimeScript RT reagent Kit	TaKaRa	Cat# RR037A
Experimental models: Cell lines		
Mouse:4T1	Cell Bank of the Chinese Academic of Sciences	SCSP-5056
Human:HeLa	Cell Bank of the Chinese Academic of Sciences	SCSP-504
Experimental models: Organisms/strains		
Mouse: BALB/c (female, 5 weeks old)	Beijing HFK	Cat#11002A
Oligonucleotides		
Primer:GPX4 forward: TGTGCATCCCGCGATGATT	GENEWIZ	N/A
Primer:GPX4 forward: CCCTGTACTTATCCAGGCAGA	GENEWIZ	N/A
Primer: β-actin forward:GGCTGTATTCCCCTCCATCG	GENEWIZ	N/A
Primer: β-actin reverse:CCAGTTGGTAACAATGCCATGT	GENEWIZ	N/A
Software and algorithms		
Graphprism 8.0	Graphpad	https://www.graphpad.com/resources
ModFit LT32	ModFit LT	https://www.vsh.com/products/mflt/index.asp

EXPERIMENTAL MODEL AND STUDY PARTICIPANT DETAILS

Unless specified, chemicals were purchased from several commercial companies and used without further purification. $FeCl_3$, NaH_2PO_4, Na_2SO_4 and hydroxylamine hydrochloride were purchased from Aladdin Company (Shanghai, China). $HAuCl_4 \cdot 3H_2O$, Polyethyleneimine, sodium citrate and NaOH were all purchased from Macklin Chemical Co. (Shanghai, China). $NaBH_4$ was purchased from Tianjin Fengchuan Chemical Reagent Co., Ltd. The murine breast tumor cell line (4T1) and human cervical carcinoma cell line (HeLa) were purchased from the National Collection of Authenticated Cell Cultures (Shanghai, China). The cell lines have been authenticated and were tested for mycoplasma contamination. Roswell Park Memorial Institute-1640 (RPMI-1640) medium and trypsin-EDTA solution,0.25% (without phenol red),

were purchased from Beijing Solarbio Science & Technology Co., Ltd. The fetal bovine serum (FBS) was purchased from Cell-Box Co. Balb/c mice used in animal experiments were purchased from BEIJING HFK BIOSCIENCE CO.LTD. The animal experiment has passed the ethical review of Henan Institute of Medical and Pharmaceutical Sciences, No. 2022-24.

METHOD DETAILS

Preparations of magnetic vortex naked-nano-donut (MVD)

The synthesis approach of the basic non-magnetic naked-nano-donut was a simple hydrothermal method derived from previous work.[58] 259.2 mg $FeCl_3$, 1.728 mg NaH_2PO_4 and 6.248 mg Na_2SO_4 were mixed in 80 mL aqueous solutions with distilled water. After vigorous stirring for 30 min, the mixture was transferred into a hydrothermal reactor liner with a capacity of 100 mL for hydrothermal treatment at 220°C in an oil bath for 24 h. The autoclave was allowed to cool to room temperature at the end of the experiments. The orange precipitate was separated by centrifugation (10000 r/min), washed with distilled water and absolute ethanol 8 times, and dried under vacuum at 80°C for following use.

For the reduction experiment on powdered naked-nano-donut, the as-prepared nanoparticles (1.0 g) were flatted on the bottom of a quartz boat, which was placed in the middle part of a quartz tube and kept horizontally in the furnace. A mixed gas of 5% hydrogen and 95% argon was passed through the quartz tube at a rate of 1.0 L/min for 20 min to remove other gases. Then the system was heated to 400 °C at a speed of 10°C/min and kept at that temperature for 2 h before being cooled down to room temperature.

Preparations of GMVD

On the basis of MVD, colloidal gold was added to synthesize GMVD. First, colloidal gold particles are prepared.[59] Add $HAuCl_4 \cdot 3H_2O$ (1 mL, 1 wt %) to ultrapure water (90 mL). After mixing for 1 min, sodium citrate (2 mL, 38.8 mM) was added and stirred for an additional minute. Then 1 mL of 0.075 wt % $NaBH_4$ in aqueous sodium citrate (38.8 mM) was added, stirring the reaction mixture for 5 min.

The initially formed MVD were heated at 90°C for 2 h in the presence of PEI solution (4 g/L) to self-assemble on their surface with PEI. The collected MVD-PEI particles were rinsed 5 times with Milli-Q water and suspended in 80 mL of Milli-Q water, yielding a suspension of NPs (3.2 g/L, pH~7). A 2 mL volume of the above MVD-PEI was then stirred for 2 h with 90 mL of 2 nm colloidal gold particles. The MVD-PEI-Auseed particles were magnetically separated from excess Au colloid solution and rinsed 5 times with Milli-Q water. The particle surfaces were then functionalized again with PEI by heating in a 60°C oven for 1 h in the presence of a 5 g/L PEI solution, followed by rinsing 5 times and dispersion in 20 mL of Milli-Q water with an ultrasonic probe.

Colloidal gold particles were next grown by iterative reduction of $HAuCl_4$ onto the MVD-PEI-Auseed-PEI. Twenty milliliters of Au-seeded nanoring were mechanically stirred with 110 mL of 0.01 M NaOH (Ph~11.5). A first iteration of 0.5 mL of 1% $HAuCl_4$ was added along with 0.75 mL of 0.2 M $NH_2OH \cdot HCl$, followed by 0.5 mL of 1% $HAuCl_4$ and 0.25 mL of 0.2 M $NH_2OH \cdot HCl$ for the subsequent iterations. A total of up to five iterations were made, with 10 min in between iterations. The GMVD was then magnetically separated from the reaction mixture, rinsed 5 times, and dispersed in 20 mL of Milli-Q water with an ultrasonic probe.[60]

Characterization

GMVD is separated and purified by magnetic adsorption. Particle morphology and crystal lattice were measured using a field-emission scanning electron microscope (FE-SEM, JEOL, JSM-6700F, 15 kV, Tokyo, Japan) and a transmission electron microscope (TEM, Hitachi, HT7800, 120 kV, Tokyo, Japan). The magnetic properties of the NPs were measured at 300 K using a superconducting quantum interference device (SQUID) magnetometer (Quantum Design MPMS-5S, Quantum Design Inc., San Diego, USA). At room temperature, X-ray diffraction (XRD) was measured using a Bruker D8 Advance diffractometer (Bruker GmbH, Karlsruhe, Germany). The UV-Vis spectrum was obtained using a NanoDrop 2000 (Thermo Fisher Scientific Inc., USA), and XPS were measured using a Thermo Scientific ESCALAB Xi+ instrument. The 808-nm NIR laser source LWIRL808-5F (Beijing Laserwave Optoelectronics Technology Co., Ltd., Beijing, China) was used for photothermal experiments. The high-frequency induction heating equipment (SPG-10A-II, Shenzhen Shuangping Technology Co., Ltd., Shenzhen, China) was used for magnetic hyperthermia experiments. The MRI data were obtained using a clinical open permanent magnet scanner (GE).

Magnetic hyperthermia effect

The magnetic hyperthermia effect was measured using the handheld infrared thermal camera (HM-TPH21Pro-3AQF, Hikmicrotech Co., Ltd., Hangzhou, Zhejiang, China). A high-frequency magnetic induction heating equipment (SPG20A, Shenzhen Shuangping, China) with 80~482 kHz frequency and 5 to 45 A heating current was used to generate the AMF. Water, non-magnetic naked-nano-donut, magnetic iron oxide nanospheres and GMVD ([Fe] = 5 mg/mL) were placed in a coil of Φ60 × 7 turns and measured at different powers of 15,20,25,30 A to observe the temperature changes.

And then specific absorption rate (SAR) was calculated using the following equation:[61]

$$SAR = C \frac{\Delta T}{\Delta t} \frac{1}{m_{Fe}} \qquad \text{(Equation 1)}$$

Where C is the constant value of the specific heat capacity of water, $\Delta T/\Delta t$ is temperature change per unit of time, and m_{Fe} is the Fe concentration.

Photothermal effect

Photothermal effects were quantified by measuring temperature changes using a thermal infrared camera. For phantom studies, GMVD at concentrations of 0, 38,75,100,150 µg/mL were irradiated with an 808-nm laser at energy densities of 0.7, 1, 1.3, 1.6, and 1.9 W/cm² for 10 min, during which time the temperature of NP dispersions was monitored continuously. For *in vivo* studies, Balb/c mice bearing 4T1 tumors were intravenously injected with GMVD (0.6 mg/mL, 200 µL). Saline was used as control. Twenty-four hours after injection, the tumors were irradiated with an 808-nm laser at 1.6 W/cm² for 10 min.

Cell viability and cellular uptake

HeLa, 4T1, KYSE-150 and A-375 cells were maintained in 1640 medium supplemented with 10% FBS and cultured at 37°C in a 5% CO_2 atmosphere. Cells were first seeded in a 96-well plate at a density of 1×10^4 cells per well for 24 h. Then, GMVD was added to the wells and incubated with the cells for 12 h. One part of the cells was used to test the dark toxicity of the GMVD, while the other part was subjected to photothermal therapy (PTT) by irradiation with an 808 nm laser at 1.3 W/cm² for 10 min. Cell viability and dark toxicity were measured using the Cell Counting Kit-8 (CCK-8) assay kit (Dojindo, Tokyo, Japan). Live and dead cells were stained using a Calcein-AM/PI double stain kit (Dojindo, Tokyo, Japan) and imaged under a confocal laser microscope (Olympus, Tokyo, Japan).

As for cell uptake experiments, 4T1 cells were first seeded in a 6-well plate at 1×10^5 cells per well for 24 h; then GMVD was incubated with the cells for 12 h. Subsequently, the cells were digested with trypsin and centrifuged. The cells were fixed with glutaraldehyde fixative. After fixation, the cells were dehydrated, solidified and sectioned, and observed under a transmission electron microscope.

RNA sequencing after photothermal therapy

To confirm the changes in cellular pathways after GMVD photothermal treatment, we collected cells for RNA sequencing analysis. 4T1 cells were first seeded in a 6-well plate at 1×10^5 cells per well for 24 h; then GMVD was incubated with the cells for 12 h. The cells are then irradiated with an 808 nm laser at 1.3 W/cm² for 10 min. After continuing to culture for 24 h, the cells were collected. RNA sequencing was completed by Beijing Novogene Technology Co., Ltd., and the KEGG database was used for differential analysis.

Photothermal-triggered GMVD ferroptosis

After confirming the meaningful enrichment of ferroptosis pathways in the RNA sequencing results, we examined the occurrence of ferroptosis at the cellular level, including the production of reactive oxygen species(ROS), increases in lipid peroxides(LPO), malondialdehyde(MDA), and ferrous ions(Fe^{2+}), and changes in the related gene GPX4 in ferroptosis. 4T1 cells were seeded overnight in a 25cm² cell culture flask at a density of 5×10^5 cells per well. The cells were incubated with 600 µg/mL GMVD for 12 h and then the cells were irradiated with an 808 nm laser (1.3 W/cm²) for 10 min.

Reactive Oxygen Species Assay Kit (KeyGEN, Nanjing, China) was used to stain the RT-treated cells, which were then visualized under a confocal laser microscope.

Lipid peroxidation was detected using a C11-BODIPY lipid peroxidation sensor (Dojindo, Tokyo, Japan). 4T1 cells were cultured in 6-well culture plates (1×10^5 cells per well) overnight before treating with 600 µg/mL of GMVD for 12 h. After that, the cells were irradiated with an 808 nm laser (1.3 W/cm²) for 10 min and the cells were stained with lipid peroxidation sensor staining solution for 30 min at 37°C. Then, the stained cells were visualized under a confocal laser microscope.

Malondialdehyde was detected by cellular MDA assay kit (Nanjing Jiancheng Bioengineering Institute, Nanjing, China). 4T1 cells were cultured in 48-well culture plates (2×10^4 cells per well) overnight before treating with 600 µg/mL of GMVD for 12 h. After that, the cells were irradiated with an 808 nm laser (1.3 W/cm²) for 10 min. After the cells continue to be cultured for 24 h, use a cell scraper to scrape off the cells. Transfer the cells to a plastic centrifuge tube and crush them to make a suspension. Take a sample of 0.1 mL in a 1.5 mL centrifuge tube, add the working solution prepared with the kit, and measure the absorbance of each well with a microplate reader.

Intracellular ferrous ions (Fe^{2+}) detected by FerroOrange fluorescent probe (Dojindo, Tokyo, Japan). 4T1 cells were cultured in 6-well culture plates (1×10^5 cells per well) overnight before treating with 600 µg/mL of GMVD for 12 h. After that, the cells were irradiated with an 808 nm laser (1.3 W/cm²) for 10 min and the cells were stained with FerroOrange working solution for 30 min at 37°C. Then, the stained cells were visualized under a confocal laser microscope, and measured the absorbance of each well with a microplate reader.

In vitro radiotherapy sensitization effect

The radiotherapy sensitizing effect after the addition of gold was confirmed through cell experiments, and the inhibition of cell growth by GMVD was tested, including colony formation experiments, cell cycle detection, cell migration experiments, etc. HeLa cells were seeded overnight in a 25cm² cell culture flask at a density of 5×10^5 cells per well. The cells were incubated with 300 µg/mL GMVD and 500 µg/mL Sodium Glycididazole (CMNa) for 12 h and then subjected to X-ray radiation at doses of 0, 2, 4, 6, and 8 Gy. The cells were digested and centrifuged with trypsin, washed with PBS, fixed in 70% ethanol for 12–24 h, and stained with Cell Cycle Assay Kit (KeyGEN, Nanjing, China). The fluorescence intensity of individual cells was measured and quantified on a flow cytometer (Beckman, California, USA).

HeLa cells were seeded overnight in a 25cm² cell culture flask at 5×10^5 cells per well for the colony formation assay. They were then incubated with 300 µg/mL GMVD for 12 h and treated with X-rays at doses of 0, 2, 4, 6, and 8 Gy. Next, 1×10^3 cells were seeded into 6 well plates

and cultured for 14 days. After that, the cells were fixed with methanol and stained with Giemsa. Colonies with ≥ 50 cells were counted using ImageJ software. Finally, the clone formation rate was calculated. Clone formation rate = (clone number/inoculated cell number) $\times$ 100%

For cell migration assay, HeLa cells were seeded overnight in a 6-well plate at 1×10^5 cells per well. When the cells reached about 95% confluence, they were treated with GMVD at concentrations of 0, 38, 75, 150, 300, and 600 µg/mL for 12 h and then subjected to X-ray radiation at a dose of 4 Gy. After treatment, the cell layers were scraped with a sterile 0.1 mL pipette tip to create gaps. The cells were then cultured in a serum-free medium for 24 and 48 h, and the width of the scratches was observed under a microscope. Cell migration rate = (0 h scratch width-wound width after culture)/0 h scratch width $\times$ 100%

T_2-weighted MR imaging

To demonstrate the T_2 relaxation effect of GMVD, magnetic resonance imaging examinations were performed at both the material and animal levels. All MRI experiments in this study were performed on a 0.35 Tesla (XGY-OPER, Ningbo Xingaoyi Co., Ningbo, China). In order to calculate the R_2, different concentration (0,0.05,0.1,0.2,0.4,0.8 mg/mL) of nanoring GMVD was dispersed in an aqueous solution and fixed with 0.8% agarose gel in 2-mL EP tubes. Then, the phantoms were scanned with Carr–Purcell–Meiboom–Gill (CPMG) pulse sequence in a single coronal slice with the following parameters: repetition time (TR) = 4,000 ms, echo time (TE) = 12, 24, 48, 72, 96, 108, 120, 132, 168, 180, and 192 ms, bandwidth = 50 kHz, matrix = 128 $\times$ 128, and slice thickness = 5 mm. After acquisition, T_2 fitting was carried out using the non-linear curve-fitting method and the reciprocal of T_2 is R_2.

For *in vivo* imaging, nude mice bearing 4T1 tumors were intravenously injected with 200 µL of GMVD at a concentration of 600 µg/mL. MR images were scanned at 0,1,2, 4,6,8,12 and 24 h after the injection of GMVD. Mouse was scanned with T_2W fast spins echo method at predefined time points with the following parameters: TR = 3,000 ms, effective TE = 40 ms, echo train length (ETL) = 12, matrix = 128 $\times$ 128, and field of view (FOV) = 50 mm $\times$ 50 mm. The signal intensity of the tumor and any other organs was extracted using the ImageJ software package (Rasband W., National Institutes of Health, United States) for future quantitative analysis.

Photoacoustic imaging

In order to demonstrate the photoacoustic imaging effect of GMVD, imaging examinations were performed at both the material and animal levels. The results of photoacoustic imaging (PAI) are achieved by a small animal *in vivo* multi-spectral whole-body tomography photoacoustic imaging system (iThera Medical MSOT inVision 64, Munich, Germany). For *in vitro* testing, 0,38,75,150,300,600 µg/mL concentrations of GMVD were loaded in plastic straws and tested under the wrapping of gels. For *in vivo* tests, mice were injected with 200 µL at 600 µg/mL GMVD NPs through the tail vein, and the imaging changes of the tumor site were observed at 0,2,4,6,8,10 and 24 h, respectively.

Animal models

In order to verify the synergistic tumor treatment effect of GMVD with photothermal/radiotherapy, experiments were conducted using Balb/c mice to form subcutaneous tumors. Female Balb/c mice, 5 weeks old, were subcutaneously inoculated with 5×10^6 4T1 cells on the right flank and assigned to the following six groups after tumors had formed: (1) saline as a control, (2) GMVD, (3) PTT + RT, (4) GMVD + PTT, (5) GMVD + RT, and (6) GMVD + PTT + RT. The doses for each treatment were as follows: PBS 200 µL, GMVD 200 µL at 600 µg/mL, PTT using an 808-nm laser at 1.6 W/cm^2 for 10 min, and RT at 4 Gy X-ray. PBS or GMVD were intravenously injected 8 h before treatment. Tumor volume and mouse body weight were monitored daily for 12 days after treatment using the following formula: V = length $\times$ width^2/2. Upon animal euthanization, part of tumor tissues and major organs (heart, liver, spleen, lung, and kidney) were excised, washed with PBS, and fixed in 5% formaldehyde. Tumor and tissue sections were then stained with hematoxylin and eosin (H&E) and TUNEL, and examined with a Panoramic Tissue Scanner. Another part of the tumor was grinded in a fresh state and homogenized, and the protein was extracted for western blot experiments.

QUANTIFICATION AND STATISTICAL ANALYSIS

Statistical analysis was performed with GraphPad Prism (version 8.0, San Diego, CA). T-test was used for analyzing differences between groups. The mean values $\pm$ SEM was showed in figure, and statistically signifcant differences marked with * indicate $p < 0.05$, ** indicate $p < 0.01$, *** indicate $p < 0.001$ and **** indicate $p < 0.0001$.